THE ASTROPHYSICAL JOURNAL, 436:125–143, 1994 November 20

MASS-LOSS RATES, IONIZATION FRACTIONS, SHOCK VELOCITIES, AND MAGNETIC FIELDS OF STELLAR JETS

PATRICK HARTIGAN[1]
Five College Astronomy Department, University of Massachusetts, Amherst, MA 01003
JON A. MORSE
Space Telescope Science Institute, Baltimore, MD 21218
AND
JOHN RAYMOND
Center for Astrophysics, Mail Stop 16, Cambridge, MA 02138
Received 1993 December 10; accepted 1994 March 15

ABSTRACT

In this paper we calculate emission-line ratios from a series of planar radiative shock models that cover a wide range of shock velocities, preshock densities, and magnetic fields. The models cover the initial conditions relevant to stellar jets, and we show how to estimate the ionization fractions and shock velocities in jets directly from observations of the strong emission lines in these flows. The ionization fractions in the HH 34, HH 47, and HH 111 jets are $\sim 2\%$, considerably smaller than previous estimates, and the shock velocities are ~ 30 km s^{-1}. For each jet the ionization fractions were found from five different line ratios, and the estimates agree to within a factor of ~ 2. The scatter in the estimates of the shock velocities is also small (± 4 km s^{-1}).

The low ionization fractions of stellar jets imply that the observed electron densities are much lower than the total densities, so the mass-loss rates in these flows are correspondingly higher ($\gtrsim 2 \times 10^{-7}\ M_\odot$ yr^{-1}). The mass-loss rates in jets are a significant fraction (1%–10%) of the disk accretion rates onto young stellar objects that drive the outflows. The momentum and energy supplied by the visible portion of a typical stellar jet are sufficient to drive a weak molecular ouflow.

Magnetic fields in stellar jets are difficult to measure because the line ratios from a radiative shock with a magnetic field resemble those of a lower velocity shock without a field. The observed line fluxes can in principle indicate the strength of the field if the geometry of the shocks in the jet is well known.

Subject headings: ISM: jets and outflows — ISM: magnetic fields — shock waves — stars: formation — stars: mass loss — stars: pre–main-sequence

1. INTRODUCTION

An extended period of energetic mass outflow usually accompanies the formation of a new star in our Galaxy. Outflows from young stars manifest themselves at large distances from the star ($\gtrsim 0.1$ pc) as (1) loosely collimated bipolar molecular flows which carry large amounts of energy and mass, or (2) highly collimated stellar jets that move at several hundred km s^{-1} from the star and become visible as material in the jet cools behind shock waves in the flow. There is strong evidence that accretion disks surround all of the exciting sources of stellar jets and that accretion energy powers outflows (Basri & Bertout 1993; Edwards, Ray, & Mundt 1993).

Although both bipolar molecular outflows and stellar jets were discovered almost a decade and a half ago and are now known to occur around many young stars, the relationship between these two kinds of outflow remains unclear. If stellar jets drive molecular flows, then the momentum supply rate in jets must be comparable to that in molecular flows. However, estimates of the mass and momentum in stellar jets vary by at least two orders of magnitude depending on how one interprets the existing data.

Estimates of mass-loss rates and momentum supply rates from stellar jets are typically based on one of two methods. The first procedure calculates mass and momentum loss rates from measurements of the velocity, density, and cross-sectional area of the jet. Stellar jets radiate emission lines, so it is easy to measure their radial velocities, and observations of proper motions allow us to estimate the true space velocity of the jet. If the jet is resolved spatially and we know the distance to the source, then we can easily calculate the cross-sectional area of the jet. However, to estimate a mass-loss rate, we must convert the electron density, which can be measured from the ratio of the red lines of [S II], to the total density. If the ionization fraction is low, then the electron density will be smaller than the total density, and the corresponding mass-loss rate will be higher. Taking the electron density to equal the total density, Mundt, Brugel, & Bührke (1987) found that stellar jets did not carry sufficient momentum to power molecular flows. In contrast, Raga, Binette, & Cantó (1990) and Raga (1991) reestimated the ionization fraction as $\lesssim 10\%$ using crossing shock models with simple cooling functions, and concluded that it may be possible to drive molecular flows with jets. Several recent numerical models have described how a stellar jet might transfer energy and momentum to the surrounding molecular cloud (Raga & Cabrit 1993; Raga et al. 1993; Stahler 1994; Masson & Chernin 1993; Gouveia Dal Pino & Benz 1994).

In addition to the ionization fraction, another uncertainty in mass-loss estimates is whether or not one should correct the observed density for the compression caused by the shock. Mundt et al. (1987) reduced their observed jet densities by a factor of ~ 20 to correct for compression, but Raga (1991)

[1] Present address: Rice University, Department of Space Physics and Astronomy, Houston, TX 77251-1892.

concluded that the correction for compression should be made only if the emission arises from the incident shock of a pair of shocks along a jet. We must clarify this issue before we can estimate reliable mass-loss rates from this method.

A second method for estimating mass-loss rates, normally used to interpret forbidden-line observations of T Tauri stars, uses the luminosity in a specific line such as [O I] λ6300 to estimate the number of emitting atoms in the aperture. A measure of the flow velocity then gives a mass-loss rate. Observationally this method has the advantage that it requires an estimate of the luminosity in only one line, although such observations are scarce because of the lack of reliable reddening estimates. One disadvantage with this method is that there may be oxygen atoms that do not emit [O I] λ6300, either because the temperature is too low to excite the electron to the upper state or because the temperature is too high and the oxygen is ionized. As with the first method we must decide whether or not to correct the mass-loss rates for the compression in the shock.

Large mass-loss rates in stellar jets may affect the angular momentum of young stars. A typical young star rotates slowly even though it accretes a large amount of angular momentum from a circumstellar disk; remarkably, an accretion disk appears to *slow* the rotation of the star below values found for young stars lacking disks (Edwards et al. 1993). Outflows can remove the excess angular momentum accreted from the disk if the mass outflow rate is $\gtrsim 10\%$ of the mass accretion rate (Shu et al. 1988; Shu et al. 1993). The mass outflow rates are about 10% of the mass accretion rates in FU Ori objects, which have mass accretion rates about two orders of magnitude higher than those present in T Tauri stars (Crosswell, Hartmann, & Avrett 1987). There have not been any quantitative estimates to date for the ratio of mass accretion and outflow rates in T Tauri stars. Accretion disks with outflows appear to be a universal phenomenon throughout astrophysics, so it is important to address this issue in young stars where it is possible to obtain accurate, independent measurements of the mass accretion and outflow rates.

Aside from the mass-loss rates, another outstanding question in the study of stellar jets is the peculiar emission-line spectrum seen in these objects. As early as 1980, Böhm, Brugel, & Mannery (1980) pointed out that there exist a class of very low excitation HH objects with anomalously strong lines of [O I], [S II], and [N I]. These low-excitation HH objects include both stellar jets (e.g., HH 34; HH 47), and bow shocks (e.g., HH 7). The low-excitation spectrum in the bow shock HH 7 has been interpreted as being caused by a magnetic precursor that heats molecular gas in front of the shock (Hartigan, Raymond, & Curiel 1989; Carr 1993). However, low-excitation emission lines in jets have never been satisfactorily explained theoretically, and shock models have not been used to predict the ionization fraction in jets from the observed line ratios.

Stellar jets become highly collimated within a few tens of AU from the star (Kepner et al. 1993), but the collimating agent is thus far unconstrained by observations. Most models of jet collimation use magnetic fields in some way (Lovelace, Romanova, & Contopoulous 1993; Kwan & Tademaru 1988). Although fields of several tens of microgauss have been quoted for the bow shocks of HH 34 and HH 111 (Morse et al. 1992; Morse et al. 1993a), magnetic fields have not been measured in stellar jets. Magnetic fields inhibit the compression in the postshock gas, so in principle it may be possible to infer field strengths from the line ratios observed in stellar jets. If the magnetic field is strong enough, the magnetic pressure can exceed the ram pressure in the flow, and numerical models must then include the field in order to simulate the flow dynamics correctly (e.g., Lind et al. 1989).

In this paper we present an extensive grid of over 250 radiative shock models that cover a large range of shock velocities, preshock densities, and magnetic fields. Our goal is to use the observed line ratios in stellar jets to measure the shock velocity and ionization fractions in stellar jets, and (1) estimate the ratio of the mass outflow rate to the mass accretion rate in young stars, (2) determine if stellar jets have sufficient energy and momentum to drive molecular flows, and (3) evaluate to what degree the observed line ratios and line fluxes constrain the magnetic field strength in stellar jets.

In § 2 we summarize the advantages and disadvantages of the two principal ways of measuring mass loss rates, and in § 3 we show how the accuracy of the mass-loss rates derived from electron densities are improved with a careful analysis of the observed line ratios. In § 3 we also present a series of diagrams that enable us to calculate the ionization fraction and shock velocity in a stellar jet from the ratios of any of several bright emission lines. Mass-loss rates calculated from both of the methods described above appear in § 4 for various stellar jets, and in this section we also investigate how a magnetic field affects the observed line ratios and line fluxes in planar shocks. Our conclusions appear in § 5.

2. MASS-LOSS RATES IN STELLAR JETS

2.1. *Mass-Loss Estimates Based on Electron Densities*

At first glance it seems straightforward to measure mass-loss rates in stellar jets from the expression $\dot{M} = \rho \times V \times A$, where ρ is the total density, V is the velocity of the gas with respect to the star, and A is the cross-sectional area of the jet. The cross-sectional area of a stellar jet can be measured directly from the width of the jet, and the velocity of the jet is also not difficult to measure to $\sim 20\%$. Radial velocities in jets come from observations of emission lines in the flow; tangential velocities derive from proper motions in the jet or from the radial velocity and the inclination of the flow determined by bow shock models.

Unfortunately, densities in jets are much more difficult to measure than the velocities or the areas. The red [S II] $\lambda\lambda$6716, 6731 lines are bright in stellar jets and are a reliable way to estimate electron densities, but to convert electron densities to total densities we must estimate the ionization fraction in the region where the [S II] lines radiate. In a radiative shock the ionization fraction varies in the cooling region behind the shock, first increasing as neutral material becomes ionized immediately behind the shock, and then decreasing as the ionized gas recombines. The ionization fraction can have an extended plateau or even a second maximum in the recombination regions of high velocity shocks because of the absorption of Lyman-continuum photons (§ 3.1).

Figure 1 shows how the ionization fraction, electron density, and temperature vary with distance behind the shock front for a low velocity (35 km s^{-1}) and an intermediate velocity (70 km s^{-1}) model. In both models the ionization and temperature rise quickly behind the shock front and then decline gradually as the gas cools and recombines. The compression at a point in the postshock gas is proportional to the density there and rises as the temperature falls because the pressure is nearly constant in the postshock gas. However, as the temperature drops below $\sim 10^4$ K the magnetic pressure begins to dominate the thermal

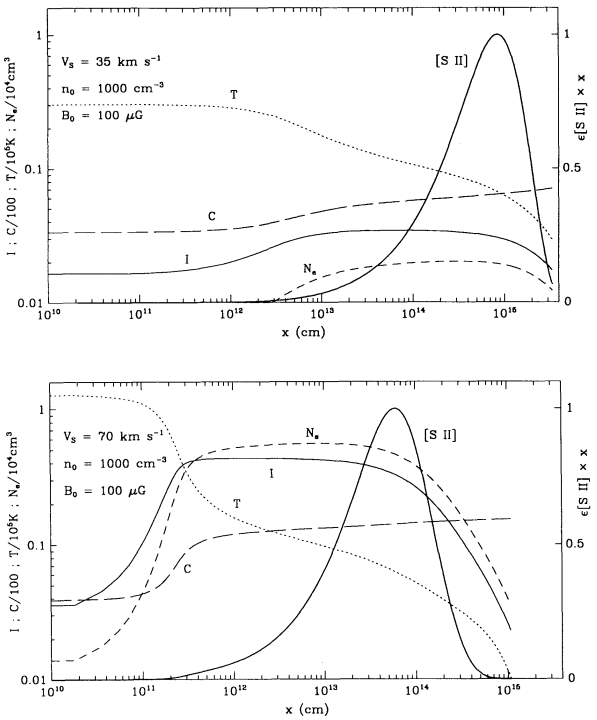

FIG. 1.—The temperature T (*dotted line*), electron density N_e (*short-dashed line*), ionization fraction $I = N_e/(N_{\rm ion} + N_{\rm neutral})$ (*solid line*), the compression $C = N_{\rm total}/N_{\rm preshock}$ (*long-dashed line*), and the [S II] $\lambda\lambda$6716+6731 emission (*heavy solid line*) appear as a function of distance x behind the shock front for a 35 km s^{-1} shock (*top*), and a 70 km s^{-1} shock (*bottom*). The curve labeled [S II] is ϵ[S II] × x, where ϵ[S II] is the emissivity (cm^3 s^{-1}) plotted vs. log (x); this quantity is proportional to the total amount of [S II] emission. The [S II] emission is on a linear scale (*right axis*) normalized to unity at the peak, and the other variables are on a log scale (*left axis*). The behavior of these variables with distance is discussed in the text.

pressure, so the compression rises only gradually as the temperature drops to $\sim 10^3$ K. The cooling distance is shorter for the 70 km s^{-1} model than it is for the 35 km s^{-1} model because the ionization fraction is larger for higher shock velocities, and the higher electron densities in the 70 km s^{-1} model cause more rapid cooling than occurs in the 35 km s^{-1} model.

The ionization fraction, compression, and electron density in Figure 1 vary by a factor of ~ 2 over the region of [S II] emission. Hence, to convert the electron density and compression measured from the [S II] line ratio to a total density we use the [S II]–weighted ionization fraction $\langle I \rangle$ defined as

$$\langle I \rangle = \int I(x) F\{[\text{S II}](x)\} dx \Big/ \int F\{[\text{S II}](x)\} dx \,, \qquad (1)$$

where $I(x)$ is the ionization fraction $[N_e(x)/N_{\rm tot}(x)]$, $F\{[\text{S II}](x)\}$ is the flux of [S II] $\lambda\lambda$6716/6731, and x is the distance behind the shock front. Our procedure for estimating densities in jets is to measure $\langle I \rangle$ from the observed line ratios and then use $\langle I \rangle$ to correct the observed electron density to the total density. In this way we determine the mass flux *at a position in the postshock gas.*

If the shock is at rest with respect to the star and lies perpendicular to the direction of the flow, then it does not matter where we measure the mass flux because the mass flux remains constant along the jet. However, if the shock *moves* with respect to the star, then the postshock velocity can be nearly as high as the preshock velocity even though the density increases by as much as an order of magnitude. In these situations the mass flux is *not* constant along the jet, but is highest in the postshock gas. Knots in stellar jets are observed to travel at a substantial fraction of the flow speed; hence, mass fluxes in stellar jets must be highly nonuniform. We must therefore take care to estimate an *average* density in the jet when calculating mass-loss rates.

Moreover, even flows that have a constant mass flux become clumpy in the presence of velocity perturbations. Figure 2, adapted from a numerical simulation of Hartigan & Raymond (1993), illustrates this process. Initially, a negative density perturbation accompanies the positive velocity perturbation so that the mass flux is constant everywhere in the flow. However, as the perturbation steepens and forms a pair of shocks (see Hartigan & Raymond 1993 for details) the mass flux becomes much higher than average in the postshock region, and lower than average in the preshock gas. Hence, mass-loss rates calculated from the densities inferred for the preshock gas are too small, and those found from the postshock gas are too large. We conclude from this exercise that the *average* mass flux lies somewhere between an estimate made from the postshock density and one made from the preshock density. In § 4 we adopt $\langle N \rangle$, a geometric mean of the preshock and postshock densities to calculate mass-loss rates:

$$\langle N \rangle = (N_{\rm preshock} \times N_{\rm postshock})^{1/2} = \langle C \rangle^{-1/2} N_{\rm postshock}$$
$$= \langle C \rangle^{1/2} \langle I \rangle^{-1} N_e \,, \qquad (2)$$

where $\langle C \rangle$ is the compression behind the shock, $\langle I \rangle$ is the ionization fraction, and N_e is the observed electron density in the postshock gas. As in the case of the ionization fraction, we calculate the compression $\langle C \rangle$ as an average weighted by the flux of the red [S II] lines:

$$\langle C \rangle = \int C(x) F\{[\text{S II}](x)\} dx \Big/ \int F\{[\text{S II}](x)\} dx \,. \qquad (3)$$

The mass-loss rate is then

$$\dot{M}_{\rm out} = \mu m_{\rm H} \langle N \rangle V_j A \,, \qquad (4)$$

where the mean molecular weight μ is ~ 1.24 for gas with cosmic abundances.

We will show in § 4 that ionization fractions and densities can be measured to within a factor of ~ 2 for most stellar jets, but uncertainties caused by the clumpy nature of the outflow amount to another factor of ~ 2 ($\langle C \rangle$ is $\lesssim 20$ for most jets) in the mass-loss rate. The above method asssumes that a single shock velocity characterizes the emission in the jet, an assumption that is justified if the shock velocities predicted from different line ratios are the same. We must also assume that all of the material in the jet passes through the shocks; any free-flowing gas down the axis of the jet or exterior to the jet will not radiate and will be undetectable. The above method has the advantages that it uses all the information present in the spectrum to estimate the mass-loss rate, and we can employ line ratios that are insensitive to the reddening and are easy to measure. The method is also independent of the physical mechanism that produces the shocks in the jet.

2.2. *Mass-Loss Rates Based on Luminosities of Forbidden Lines*

Forbidden lines are optically thin, so their luminosities provide an alternate means to estimate mass loss rates from young stars (Edwards et al. 1987; Cabrit et al. 1990). For example, the luminosity $L_{6300,6363}$ of the [O I] $\lambda\lambda$6300, 6363 lines is related to the total number of neutral oxygen atoms in

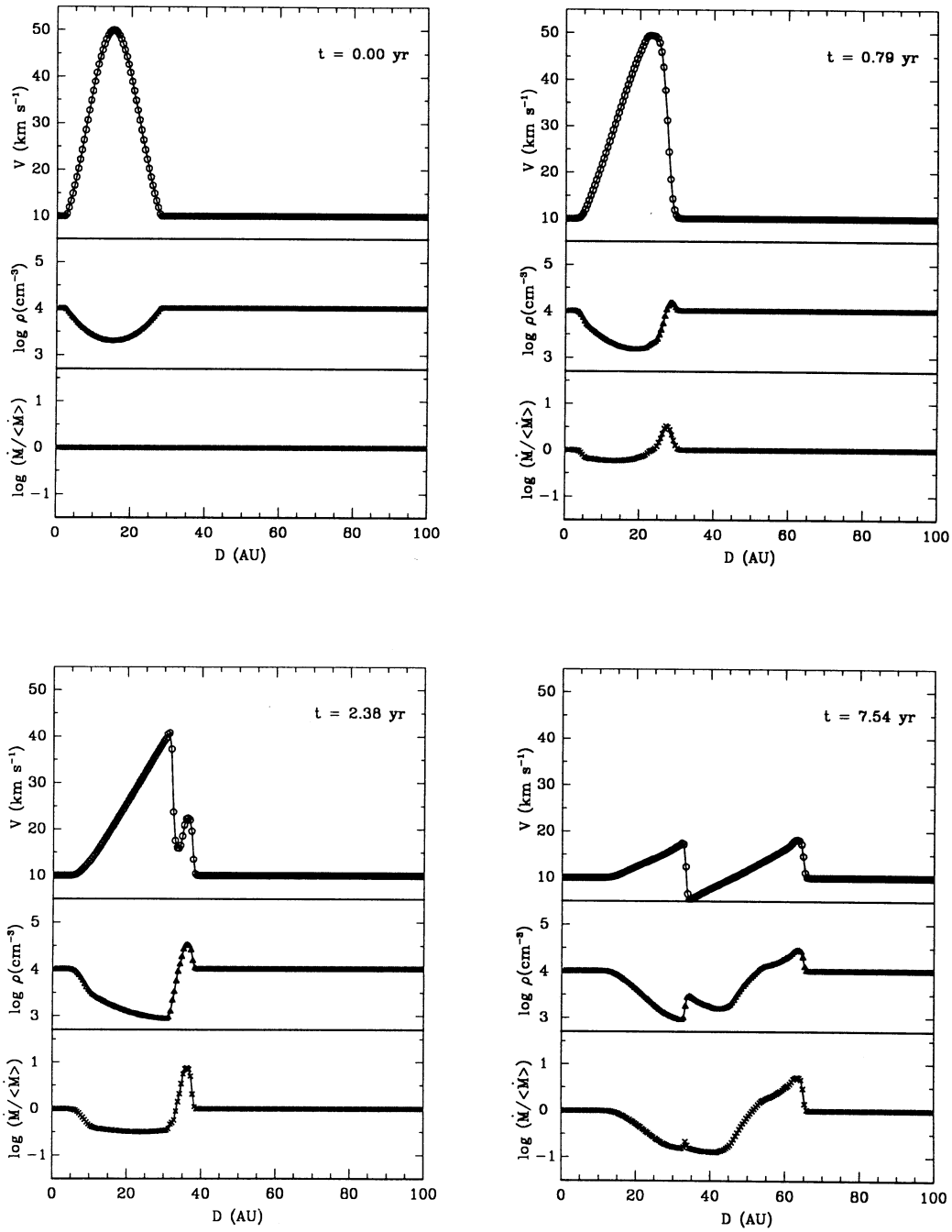

FIG. 2.—This figure, adapted from Fig. 3 of Hartigan & Raymond (1993), shows that a flow that begins with a constant mass flux evolves into a clumpy flow if the velocity is not constant. From top to bottom, each panel shows the velocity, density, and the mass-loss rate ($\rho \times V$) vs. distance for a model jet. At time zero (*upper left panel*) there is a positive velocity perturbation and a corresponding negative density perturbation that combine to produce a constant mass flux. As the flow evolves, fast material overtakes slow material (*upper right panel*) and forms a pair of shocks (*lower panels*). The mass flux in the postshock material is much greater than the average for the flow, and that for the preshock material is less than the average. Hence, to obtain an accurate value for the *average* mass flux, we must use a density that is intermediate between the preshock and postshock densities.

the excited state η_2 and in the ground state η_1 within the aperture by the equation

$$L_{6300,6363} = \eta_2 A_{21} h\nu_{21} = \eta_1 N_e C_{12} h\nu_{21} , \quad (5)$$

where

$$C_{12} = \frac{8.63 \times 10^{-6} \Omega_{12} e^{-(h\nu_{12}/kT_e)}}{g_1 T_e^{1/2}} \text{ cm}^3 \text{ s}^{-1} \quad (6)$$

and A_{21}, Ω_{12}, g_1, N_e, and T_e are the Einstein A-coefficient, collision strength, ground state statistical weight, electron density, and electron temperature, respectively. The above equations assume that the electron density is much lower than the critical density ($\sim 10^6$ cm^{-3} for this transition). The average temperature for [O I] λ6300 emission in shocks is $\sim$8200 K. Using this value for T_e, cosmic abundances (see Hartigan, Raymond, & Hartmann 1987), and the atomic

parameters for [O I] in Mendoza (1983), we obtain

$$L_{6300,6363} = 7.35 \times 10^{-56} \eta_{\rm tot} \left(\frac{N_e}{10^3 \text{ cm}^{-3}}\right) L_\odot , \quad (7)$$

where $\eta_{\rm tot}$ is the total number of atoms in the aperture. The total mass is then

$$M = \mu m_{\rm H} \eta_{\rm tot} = 1.42 \times 10^{-2} \left(\frac{N_e}{10^3 \text{ cm}^{-3}}\right)^{-1} \left(\frac{L_{6300,6363}}{L_\odot}\right) M_\odot , \quad (8)$$

and the mass-loss rate is

$$\dot{M} = MV/l , \quad (9)$$

where V is the velocity of the jet and l is the length of the jet contained within the aperture. Replacing the length l and the velocity V with their projections in the plane of the sky and combining the above equations, we find

$$\dot{M} = 5.95 \times 10^{-8} \left(\frac{N_e}{10^3 \text{ cm}^{-3}}\right)^{-1} \left(\frac{L_{6300}}{10^{-4} L_\odot}\right) \left(\frac{V_\perp}{100 \text{ km s}^{-1}}\right) \times \left(\frac{l_\perp}{10^{16} \text{ cm}}\right)^{-1} M_\odot \text{ yr}^{-1} , \quad (10)$$

where we have noted that $L_{6300} = 0.75 \times L_{6300,6363}$.

The expression for the mass-loss rate in equation (10) includes several assumptions about the flow. As in the case for mass-loss rates found from the method described in § 2.1, the mass fluxes found from equation (10) will tend to be larger than the average for the jet because they refer to the densest parts of the flow. However, [O I] does not emit over the entire length of the aperture $l_\perp$, and this error tends to cancel the one made from estimating the mass fluxes in the postshock gas. The observed line luminosities must be dereddened to use equation (10), which is sometimes difficult to do around young stars obscured by dust.

Other assumptions made in the derivation are less problematic. The electron densities calculated from the [S II] lines are essentially the same as those in the [O I] emitting region because these two species radiate in the same region of the postshock gas. The assumption of negligible collisional deexcitation for [O I] λ6300 is justified in most jets because the electron densities measured from the [S II] lines are about three orders of magnitude lower than the densities required to collisionally deexcite [O I].

We can test whether or not the mass-loss rates calculated from equation (10) agree with those found from densities, velocities, and areas (eq. [4]) by applying both models to a shock with a simple geometry. Suppose we have a cylindrical jet in the plane of the sky that moves at 300 km s^{-1} with respect to the star, has a diameter of 3×10^{15} cm, a density of 1000 cm^{-3}, and a magnetic field of 100 μG. Let the flow encounter a stationary oblique shock at an incidence angle of 6°.5 so that the effective shock velocity is 35 km s^{-1}, close to the observed shock velocities in real jets (we choose a stationary oblique shock because of its geometric simplicity; this case cannot explain the large proper motions in jets, for example). The shock is an elliptical conic section, and extends over an area 2.4×10^{32} cm^2. The shock model in Figure 1 predicts $L_{6300} = 5.1 \times 10^{-6} L_\odot$ for a shock of this size, with an electron density from the [S II] lines of ~190 cm^{-3}. Taking an aperture size of 3×10^{16} cm, which is large enough to include the emission from the shock, equation (10) gives $\dot{M} = 1.6 \times 10^{-8} M_\odot$ yr^{-1}. The mass-loss rate calculated from $\rho \times V \times A$ is 7.0×10^{-9} $M_\odot$ yr^{-1} entering the shock, and 4.3×10^{-8} $M_\odot$ yr^{-1} in the region where [S II] emits. A geometric mean of the preshock and postshock mass fluxes gives $\dot{M} = 1.7 \times 10^{-8}$ $M_\odot$ yr^{-1}, essentially identical to the value found from the [O I] luminosity.

This example shows that mass-loss rates calculated from line luminosities should not differ greatly from those based on electron densities and ionization fractions. Moreover, one should not correct the mass-loss rates found from line luminosities (eq. [10]) for compression because these mass fluxes already represent an average for the material in the aperture.

3. MODEL CALCULATIONS AND RESULTS

3.1. *Planar Radiative Shock Models*

The radiative shock code used to predict emission line ratios summarized in the following sections has been described previously by Raymond (1979), Cox & Raymond (1985), and Hartigan et al. (1987). The models include all the major coolants in the ultraviolet, optical, and infrared of all the ionization states of the 13 most abundant atoms. The only modifications of atomic physics from previous papers that use this code are that we have corrected (in 1988) an error in the code that affected the fluxes of [S II], and have added (in 1993) an improved rate for charge exchange for the endothermic reaction $H^+ + N + 0.95 \text{ eV} \rightarrow H + N^+$. The new reaction rate affects the line ratios involving N and N^+ by ~15%.

In this work we present a fine grid of models that cover a wide range of shock velocities, preshock densities, and preshock magnetic fields. We have calculated shock models for 11 shock velocities (15, 20, 25, 30, 35, 40, 50, 60, 70, 80, and 90 km s^{-1}), with nine different magnetic fields (0.1, 1, 3, 10, 30, 100, 300, 1000, and 3000 μG) and three preshock densities (100, 1000, and 10,000 cm^{-3}). Some combinations of these variables do not produce shocks—for example, the lowest shock velocity calculated for the $B = 1000$ μG models with $n = 1000$ cm^{-3} was 80 km s^{-1} (the Alfvén speed in the preshock gas is 62 km s^{-1} for this case).

There are three distinct regions in a radiative shock and each must be resolved spatially if the code is to give good results. First, where neutral material enters the shock it becomes heated and gradually ionizes. This hydrogen ionizing zone also produces significant collisional excitation, which must be taken into account (especially in low-velocity shocks) to give accurate values for the Balmer lines. Collisional excitation enhances the Balmer decrement over the recombination value of 2.9. Second, the region behind the hydrogen ionization zone is where atomic species such as [O III], [O II], and [N II] cool and recombine. These atoms are important coolants, and their abundances and cooling rates must be followed by the code. Finally, the shock model must carefully monitor the Lyman-continuum photons produced in the hottest regions behind the shock. These photons ionize material both upstream from the shock, where they preionize the incident H, and downstream into the cooling region where they can reionize the H and eject electrons. Collisions of O I, N I, S II, and other species with these photoionized electrons produce forbidden line radiation when the atoms decay. The present code allows as many as 1000 steps, which were parsed to spatially resolve each of the three zones described above.

Stellar jets typically consist of a series of knots and there is evidence that velocity variability may account for at least some of the shocks along jets (e.g., Reipurth 1989a). The dispersion of proper motions and radial velocities in stellar jets suggests that on average an atom in a jet encounters a new shock wave every 200 yr or so (Heathcote & Reipurth 1992; Eislöffel & Mundt 1992; Reipurth, Raga, & Heathcote 1992). For this reason we have allowed the gas to cool for 200 yr in all of our models. This restriction affects only the lowest shock velocities and lowest densities because the other models cool to below 1000 K and no longer emit significant forbidden line radiation after 200 yr. Models with low ($\lesssim$40 km s^{-1}) shock velocities cool more slowly than those with intermediate (40 km s^{-1} $\lesssim$ V_s $\lesssim$ 100 km s^{-1}) velocities because the ionization fraction is lower in the low-velocity shocks, and fewer electrons result in lower rates of collisional excitation. Shocks with low preshock densities also cool more slowly than dense shocks because line cooling (proportional to n^2) decreases more rapidly than the rate of incident kinetic energy (proportional to n) as the density falls.

Lyman-continuum photons that travel ahead of the shock preionize H, and in turn, the amount of Lyman-continuum radiated by the shock depends upon the ionization fraction of the incident H. In our models we solve for the "equilibrium" preionization by iterating until the H preionized fraction agrees with the ionization fraction present at the end of the simulation (t = 200 yr). Typically about three iterations were necessary for the ionization fraction to converge to within 5%, but models with large magnetic fields required as many as 11 iterations to converge. In all, we calculated a total of over 1000 shock models.

We assume that the cooling all comes from atomic gas. Molecular hydrogen emission has been observed near some optical jets, but H_2 usually lies along the edges of the jet. For example, the H_2 emission near HH 8 and near HH 10 has low radial velocities (Carr 1993) and probably exists as clumps along the edges of a cavity opened by the jet. Similarly, the H_2 emission found by Zealey, Suters, & Randall 1993 in HH 47 lies somewhat to the north of the blueshifted jet. However, some very young objects may have molecular jets (e.g., L1448; Davis et al. 1993), and the models in this paper should not be used to estimate ionization fractions and mass loss rates in these systems.

3.2. *Measuring Shock Velocities and Ionization Fractions in Jets from Line Ratios*

The [S II]–weighted ionization fraction $\langle I \rangle$ (eq. [1]) is plotted against various emission line ratios for each of our shock models in Figures 3–7. The ratios [O I] λ6300/Hα, [S II] $\lambda\lambda$6716+6731/Hα, [N I] $\lambda\lambda$5198+5201/Hβ, and [N II] λ6583/[O I] λ6300 are excellent diagnostics of the ionization fraction because these ratios are insensitive to reddening corrections and use the brightest emission lines visible in jets. The ratio [N I] $\lambda\lambda$5198+5201/[N II] λ6583 is more sensitive to reddening but is independent of the elemental abundances.

Shock velocities for each of the above line ratios appear in Figures 8–12 (by "shock velocities" we mean the component of the velocity vector that is perpendicular to the surface of the

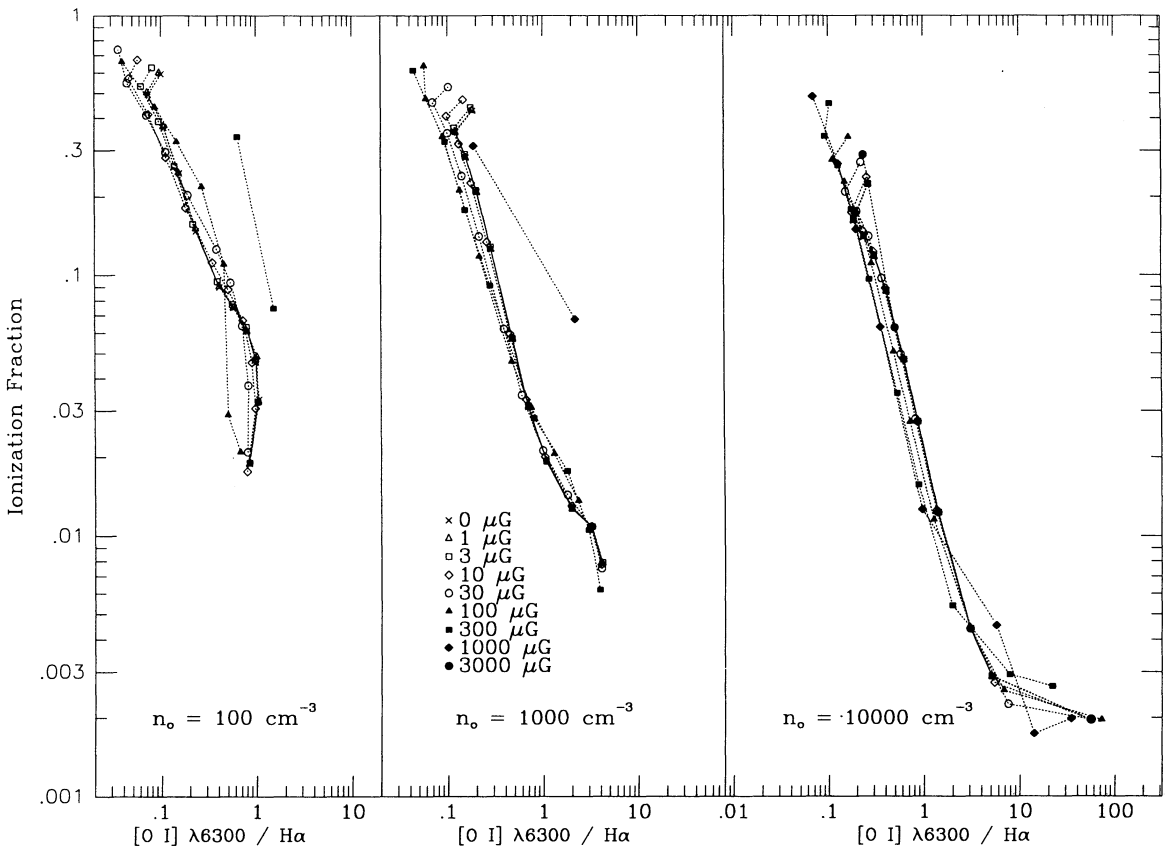

FIG. 3.—The [S II]–weighted ionization fraction, which is the ratio of the electron density measured from the red lines of [S II] to the total density, appears as a function of the line ratio [O I] λ6300/Hα for three preshock densities and nine preshock magnetic fields. The values listed for the magnetic fields refer to the component of the field that lies parallel to the surface of the shock. When the ratio [O I] λ6300/Hα > 1 the ionization fraction is $\lesssim$0.02.

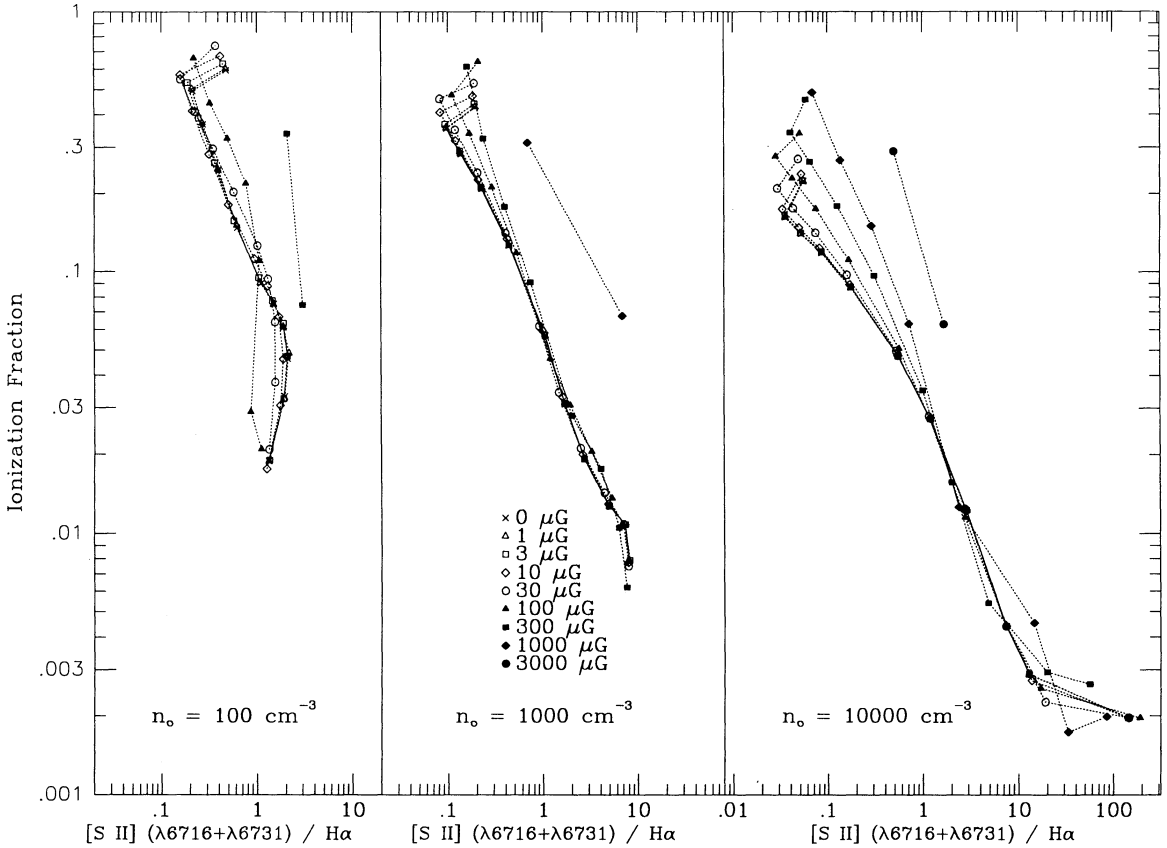

FIG. 4.—Same as Fig. 3, but for [S II] λλ6716 + 6731/Hα

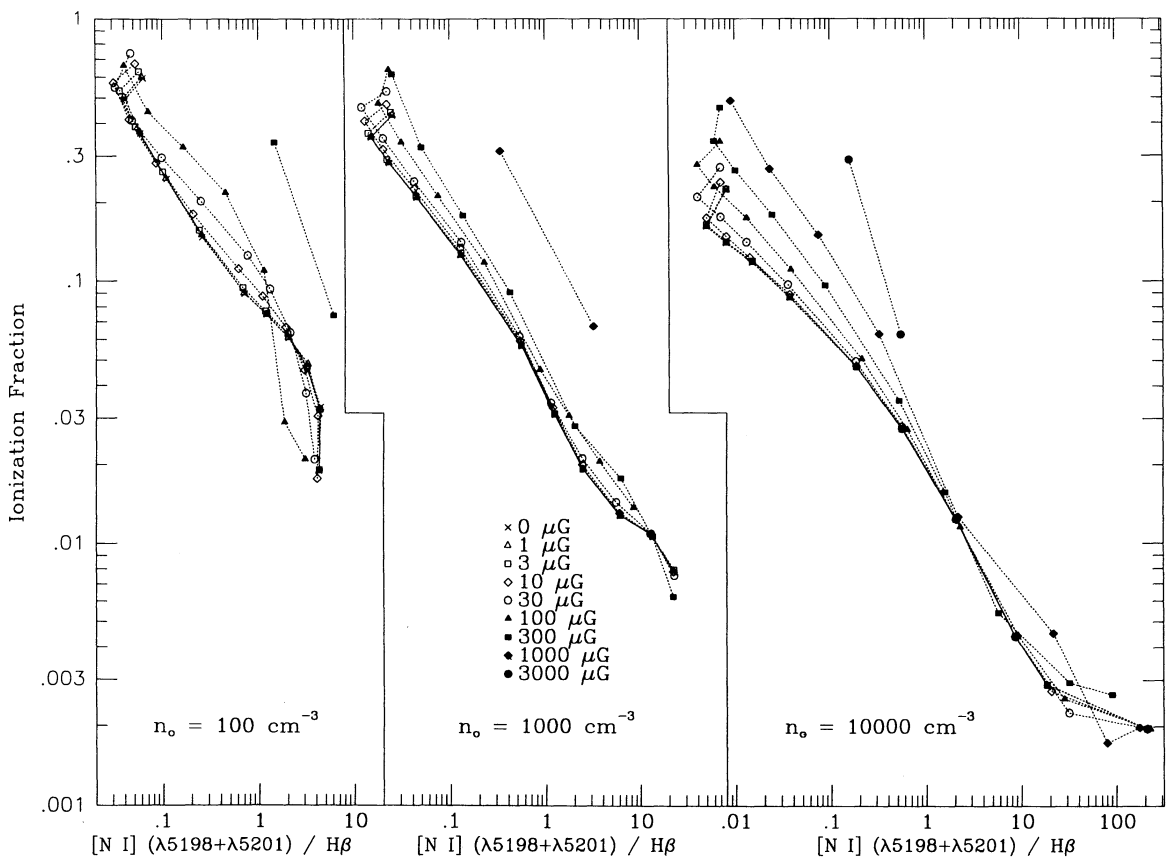

FIG. 5.—Same as Fig. 3 but for [N I] λλ5198 + 5201/Hβ

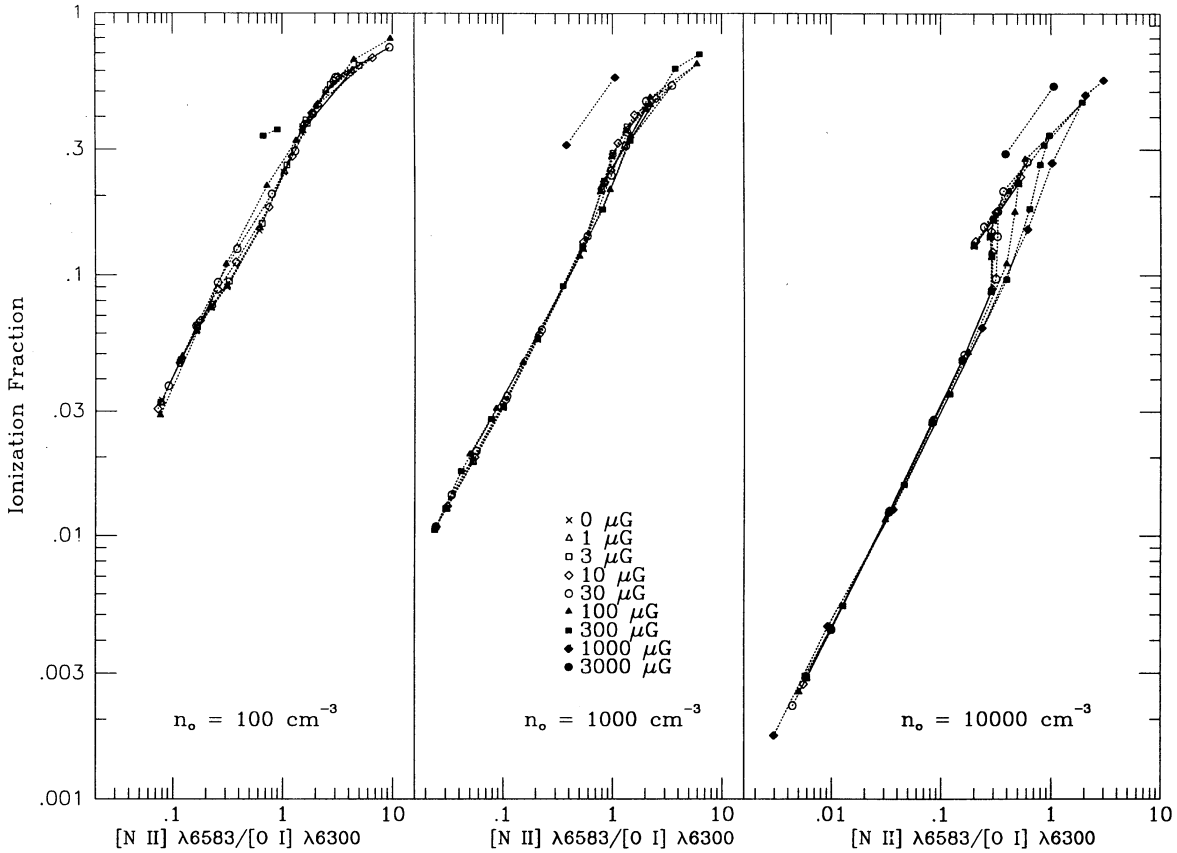

FIG. 6.—Same as Fig. 3 but for [N II] λ6583/[O I] λ6300. This line ratio is insensitive to the strength of the magnetic field and the preshock density.

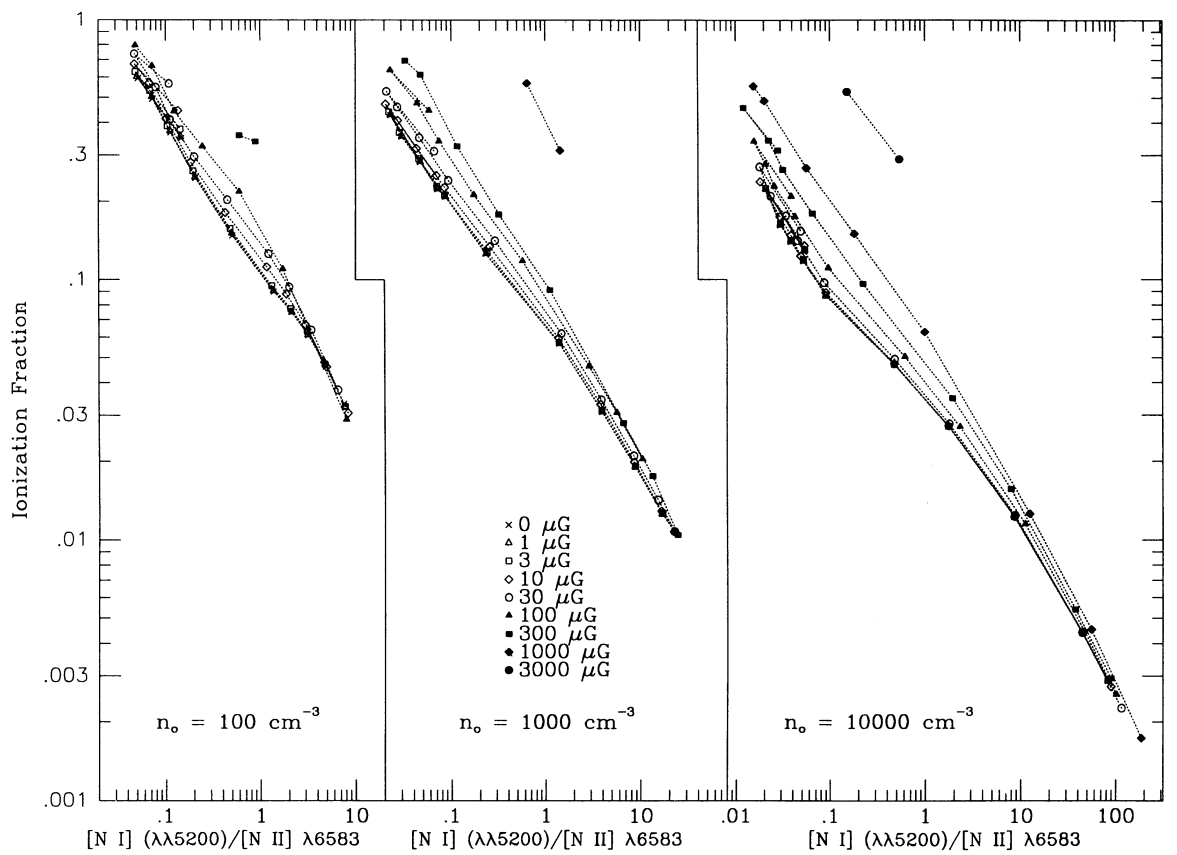

FIG. 7.—Same as Fig. 3 but for [N I] λλ5198 + 5201/[N II] λ6583. This line ratio is independent of any abundance anomalies.

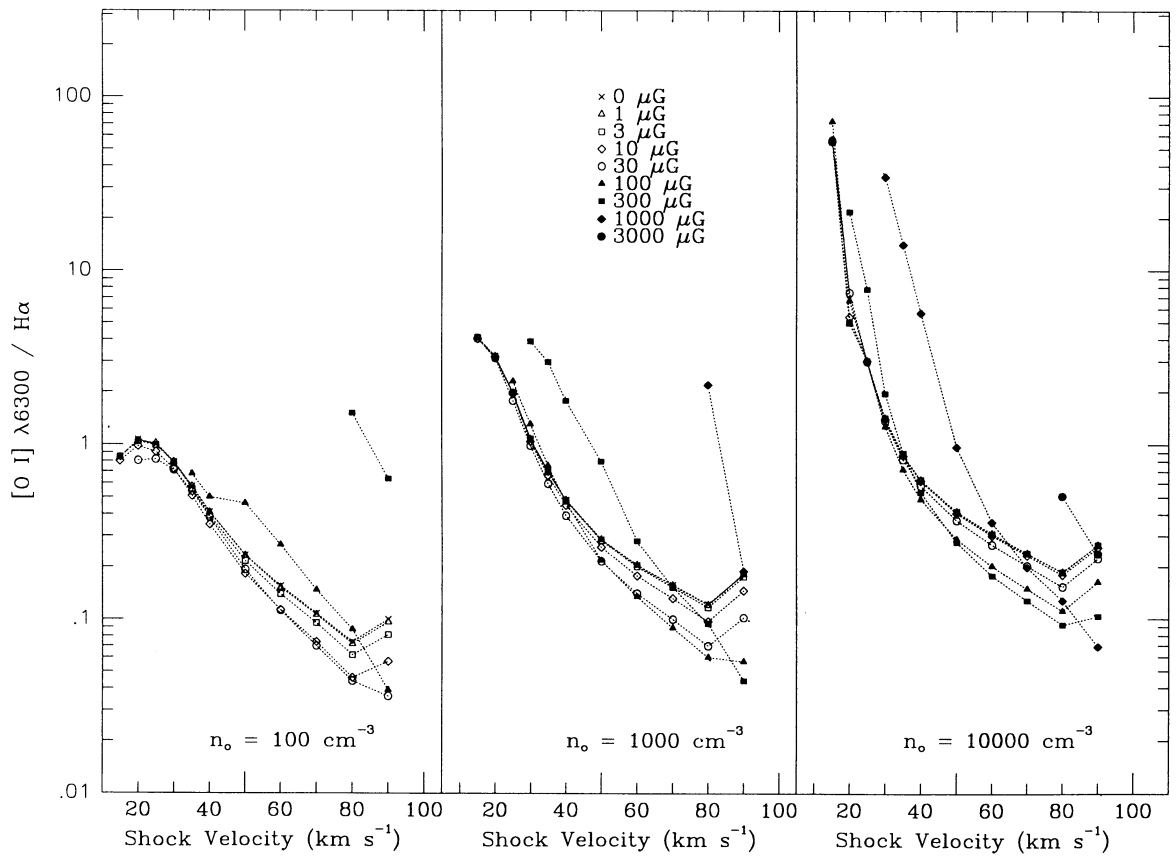

FIG. 8.—The ratio [O I] λ6300/Hα appears as a function of the shock velocity for three preshock densities and nine preshock magnetic fields. This line ratio increases as the shock velocity decreases.

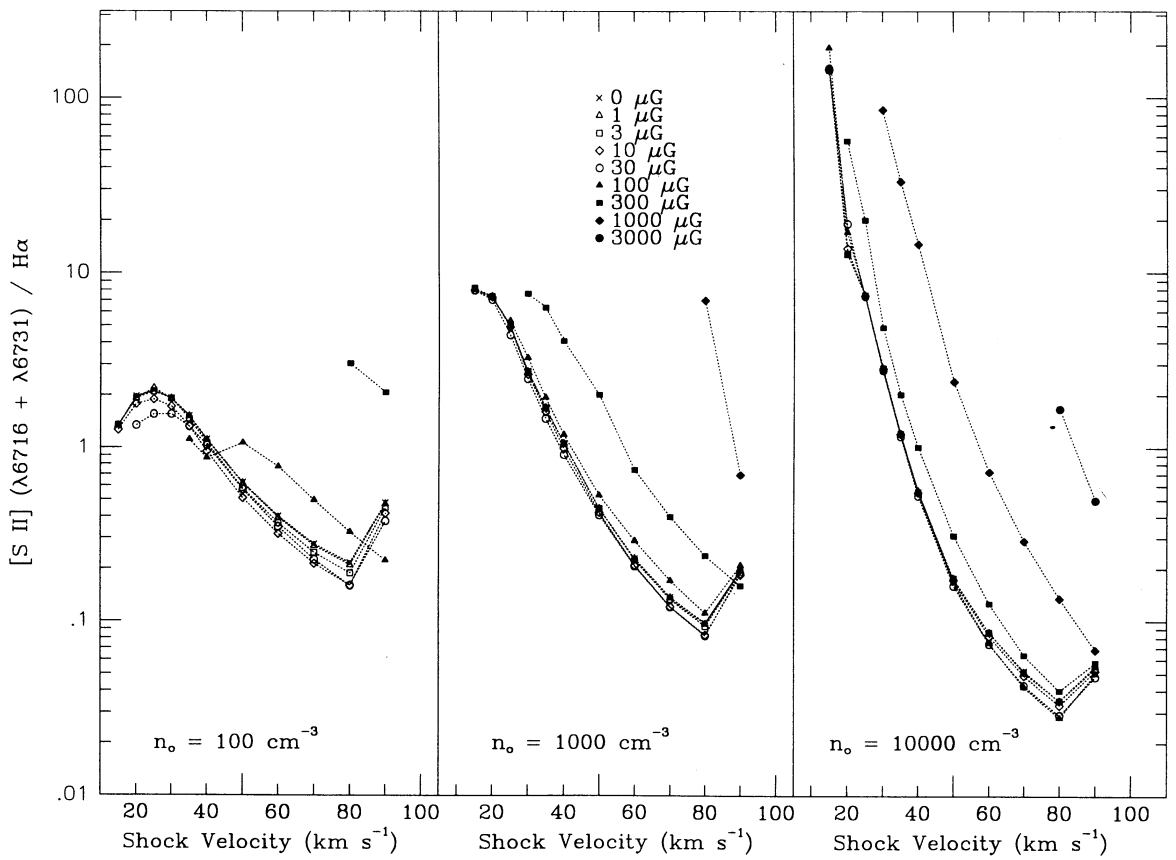

FIG. 9.—Same as Fig. 8 but using the ratio [S II] λλ6716 + 6731/Hα

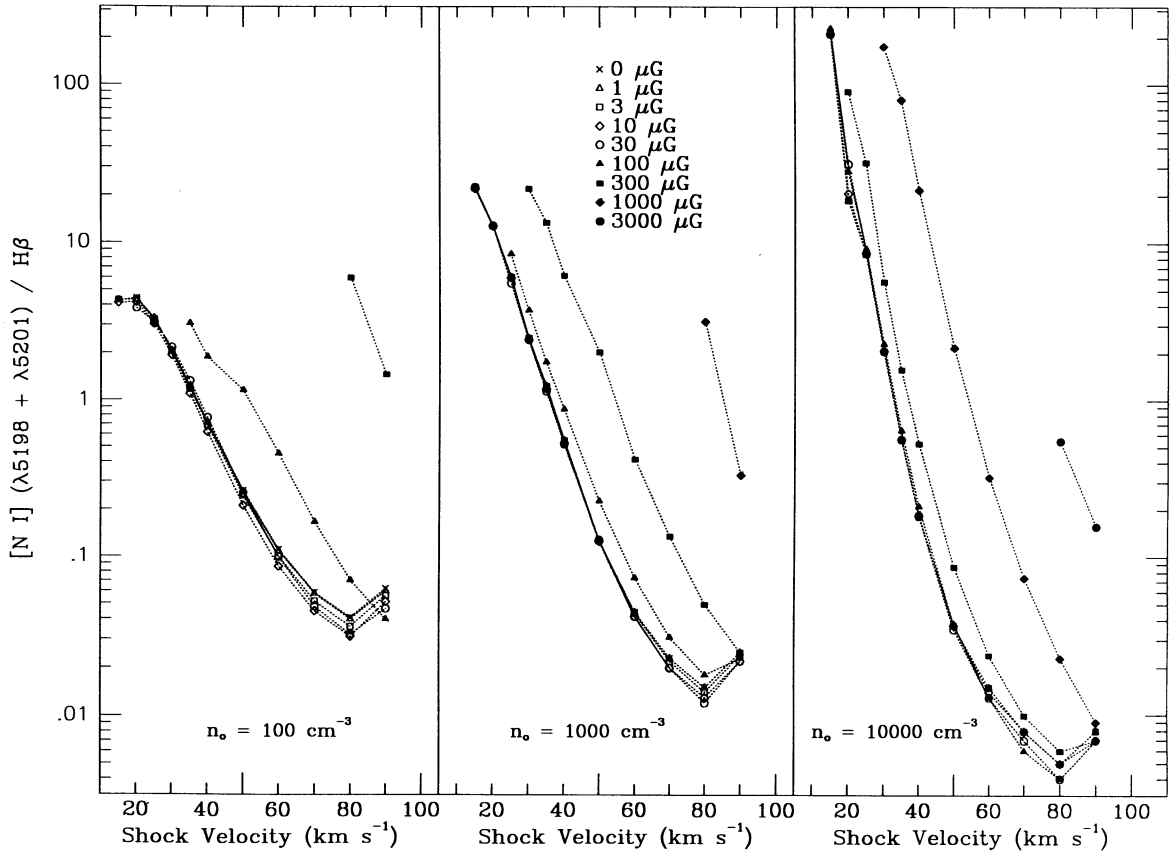

FIG. 10.—Same as Fig. 8 but for [N I] λλ5198 + 5201/Hβ

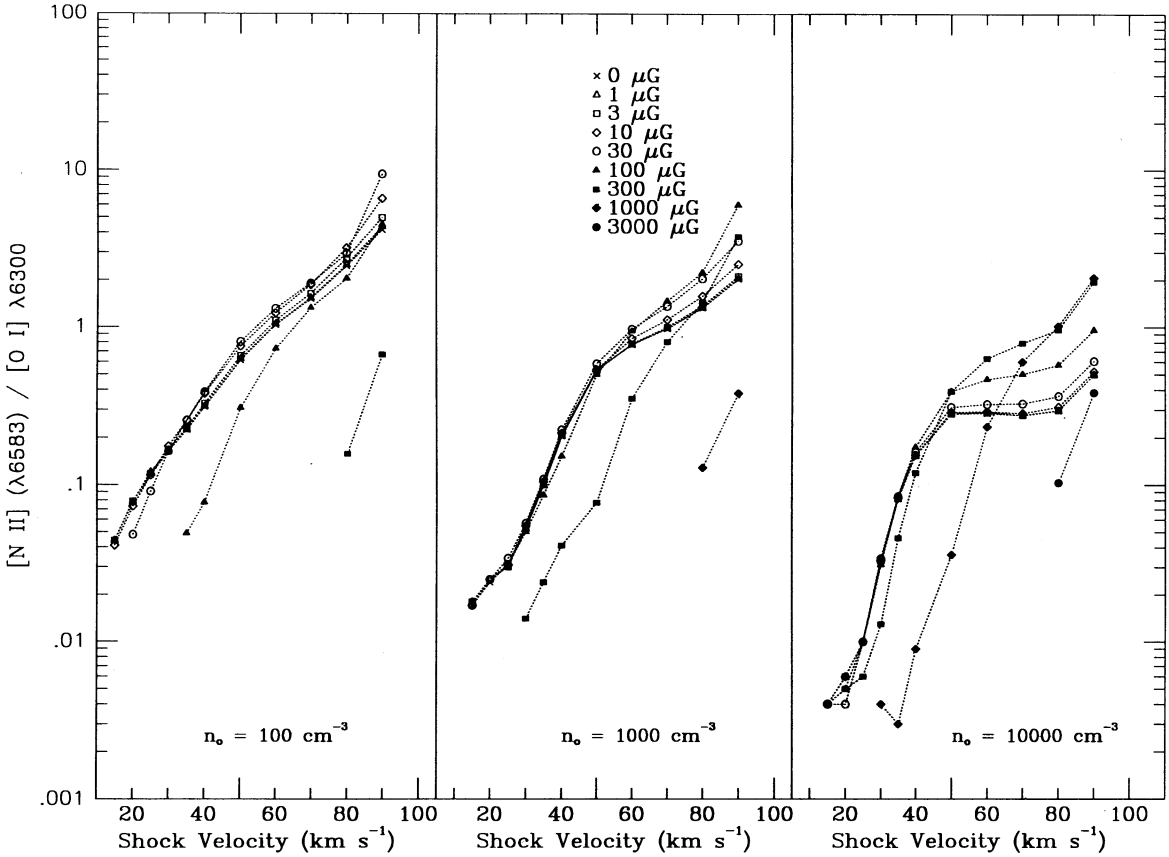

FIG. 11.—Same as Fig. 8 but for [N II] λ6583/[O I] λ6300

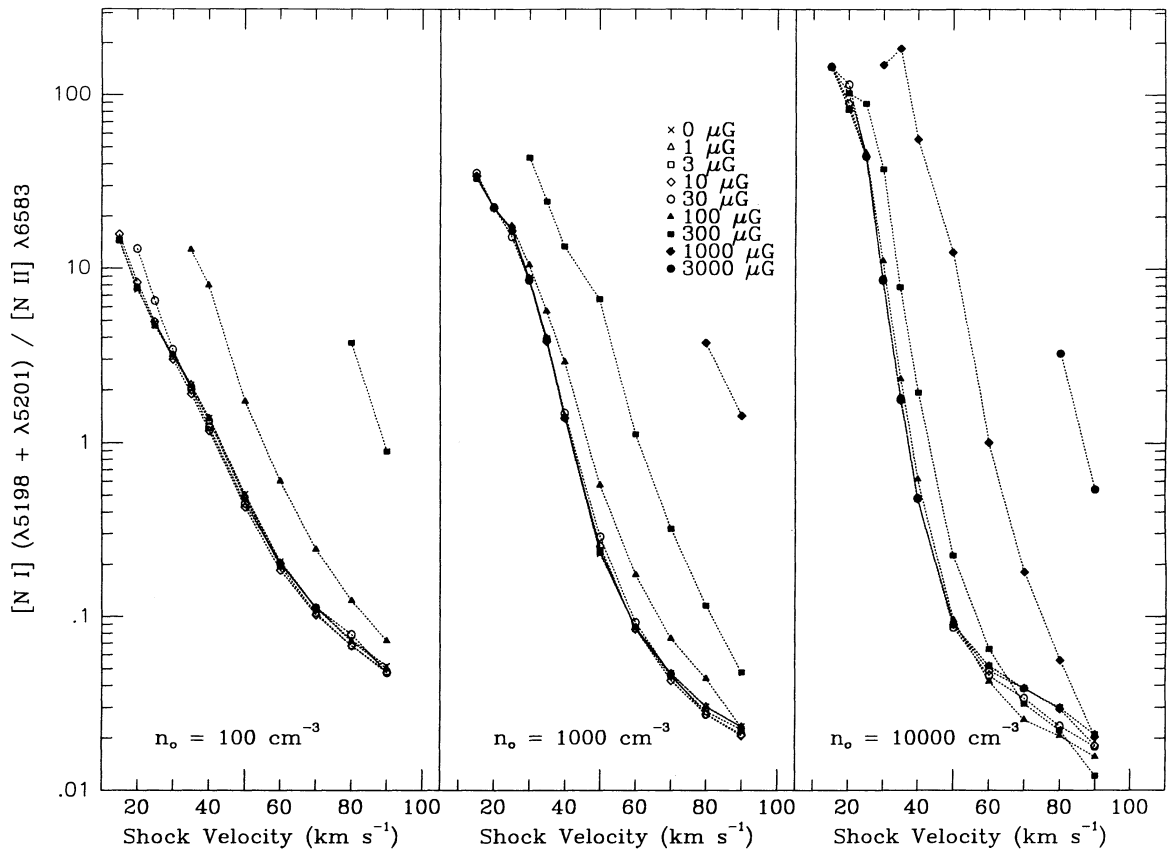

FIG. 12.—Same as Fig. 8 but for [N I] λλ5198 + 5201/[N II] λ6583

shock). Shock velocities are easy to measure accurately from any of these line ratios. The [O II] λλ3726 + 3729/[O I] λ6300 ratio in Figure 13 is less useful because the [O II] λλ3726 + 3729 lines have a low critical density so that the flux of this doublet depends strongly on the density of the flow. The [O II] lines are also more sensitive to the preionization state of the gas than the other strong forbidden lines in jets (e.g., Hartigan, Raymond, & Meaburn 1990).

The overall behavior of the line ratios in Figures 3–13 is fairly easy to understand—low shock velocities produce little ionization, and therefore the fluxes of low-excitation lines like [O I] λ6300, [N I] λλ5198 + 5201, and [S II] λλ6716 + 6731 are enhanced relative to high-excitation lines such as the Balmer lines and [N II] λ6583. As the preshock density increases, the density becomes higher in the cooling region of the shock, and transitions with low critical densities become collisionally deexcited. For example, in Figure 5 the ratio [N I] λλ5198 + 5201/Hβ becomes smaller at larger densities because the critical density of [N I] is low (~ 1000 cm^{-3}). In contrast, ratios of lines with similar critical densities, such as [N II] λ6583/[O I] λ6300 in Figure 6, are essentially independent of the value of the preshock density. The $n_0 = 100$ cm^{-3} models with low shock velocities do not cool to below 1000 K in 200 yr. The lack of the low-temperature regions in these models reduces the fluxes of the forbidden lines relative to the Balmer lines and causes the curves for the ionization fraction in Figures 3, 4, and 5 to become nearly vertical at low shock velocities. In general, models with large magnetic fields have line ratios similar to lower velocity shocks without fields (see § 4.4).

Balmer decrements and Hβ fluxes for the models are plotted in Figures 14 and 15, respectively, and the conversion between shock velocity and ionization fraction is displayed in Figure 16.

4. APPLICATION TO SPECIFIC REGIONS

In this section we estimate mass-loss rates in three well-studied stellar jets from observations of their line ratios and line luminosities. Our choice of regions is somewhat limited, because to estimate mass-loss rates from [O I] luminosities we must have spectrophotometric measurements of the line, a value for the electron density, and a reliable estimate of the reddening. To use the line ratio method, the jet must be resolved spatially, and the emission should come from shocks that are nearly planar.

If the emission comes from unresolved bow shocks in the beam, then different line ratios will yield different shock velocities. For example, knot L in HH 111 is bow shaped and has high-excitation [O III] λ5007 at its apex (Morse et al. 1993b; Noriega-Crespo, Garnavich, & Raga 1993), and will not provide a reliable mass-loss rate for the jet. The L1551 jet shows broad velocity dispersion in the line emission (Stocke et al. 1988), and the knots HH 7–11 also appear to be bow shocks (Solf & Böhm 1987; Hartigan et al. 1987). The [S II] line ratio in the jet between HH 7 and HH 8 is in the low-density limit and cannot be used to estimate the mass-loss rate.

In what follows we assume that the component of the magnetic field $B_{\parallel}$ that lies parallel with the surface of the shock is $\lesssim 100$ μG. The effect of larger fields on the line ratios and mass-loss rates is discussed further in § 4.4.

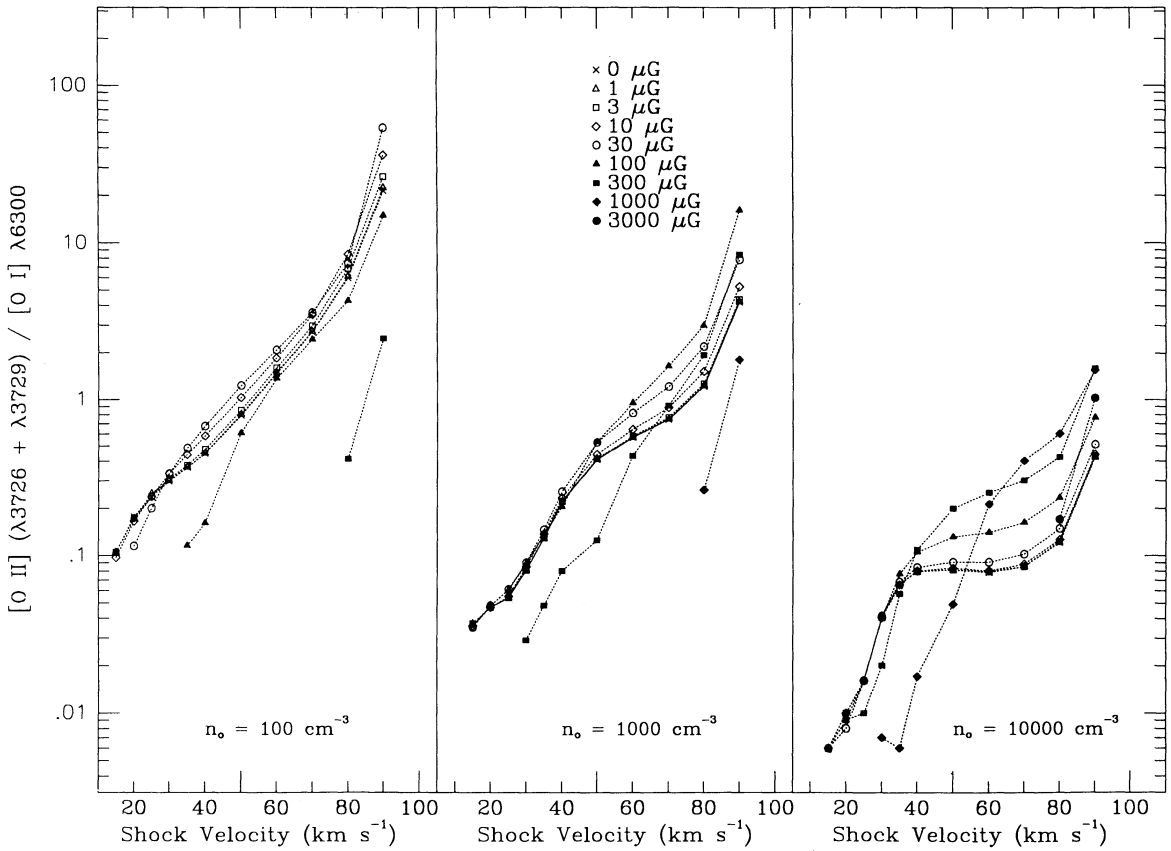

FIG. 13.—Same as Fig. 8 but using [O II] λλ3726 + 3729/[O I] λ6300. This line ratio is sensitive to the reddening corrections and the preshock density.

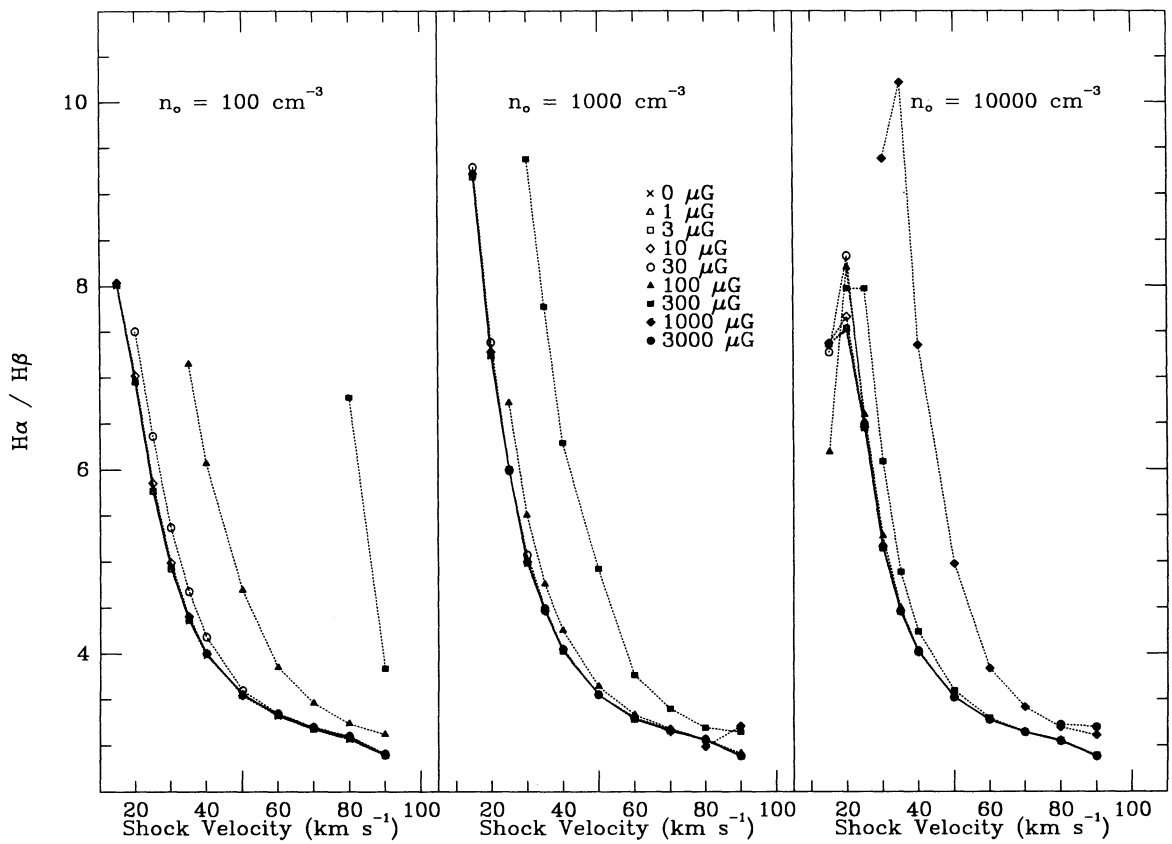

FIG. 14.—Same as Fig. 8 but using the Balmer decrement, Hα/Hβ. The Balmer decrement decreases and approaches the recombination value for high shock velocities. Collisional excitation increases the Balmer decrement at low shock velocities.

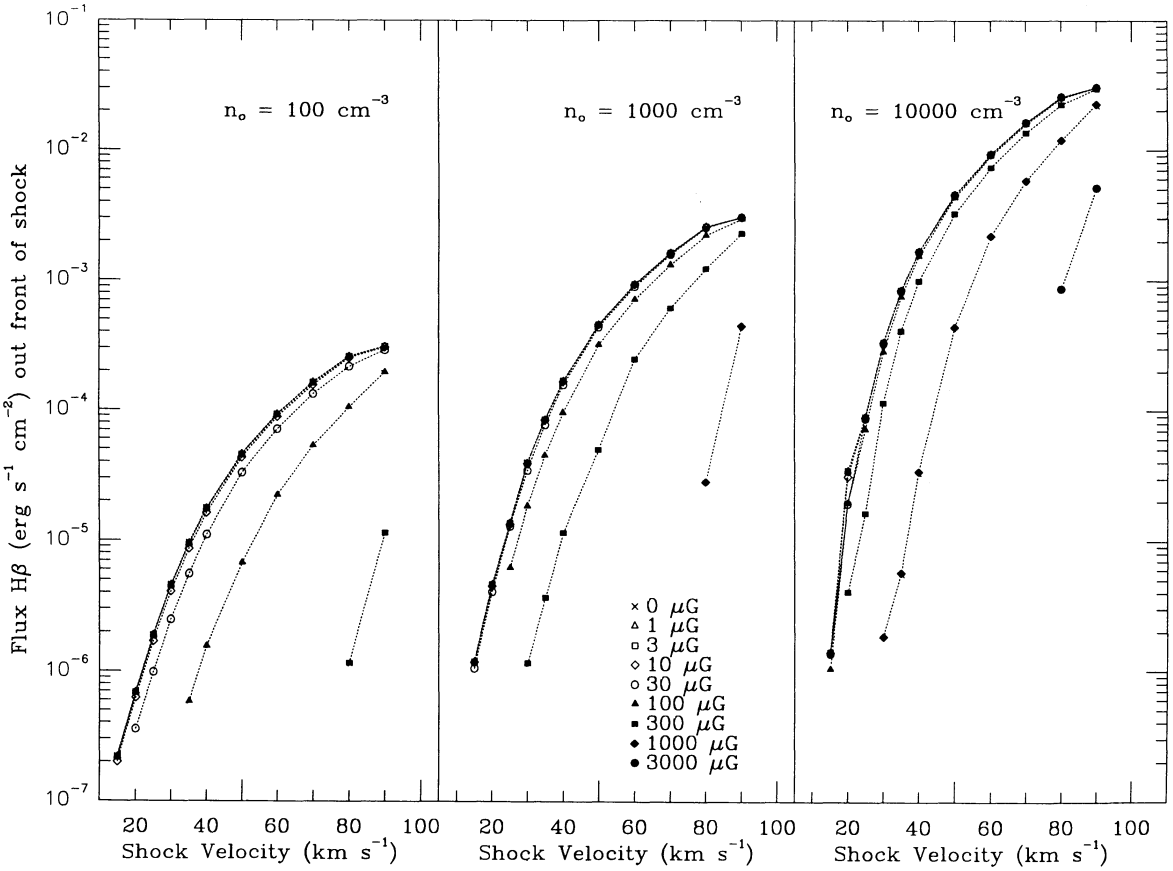

FIG. 15.—The flux of Hβ out the front of the shock appears as a function of shock velocity for each of our models. The Hβ flux increases with the preshock density and decreases when the magnetic field is large.

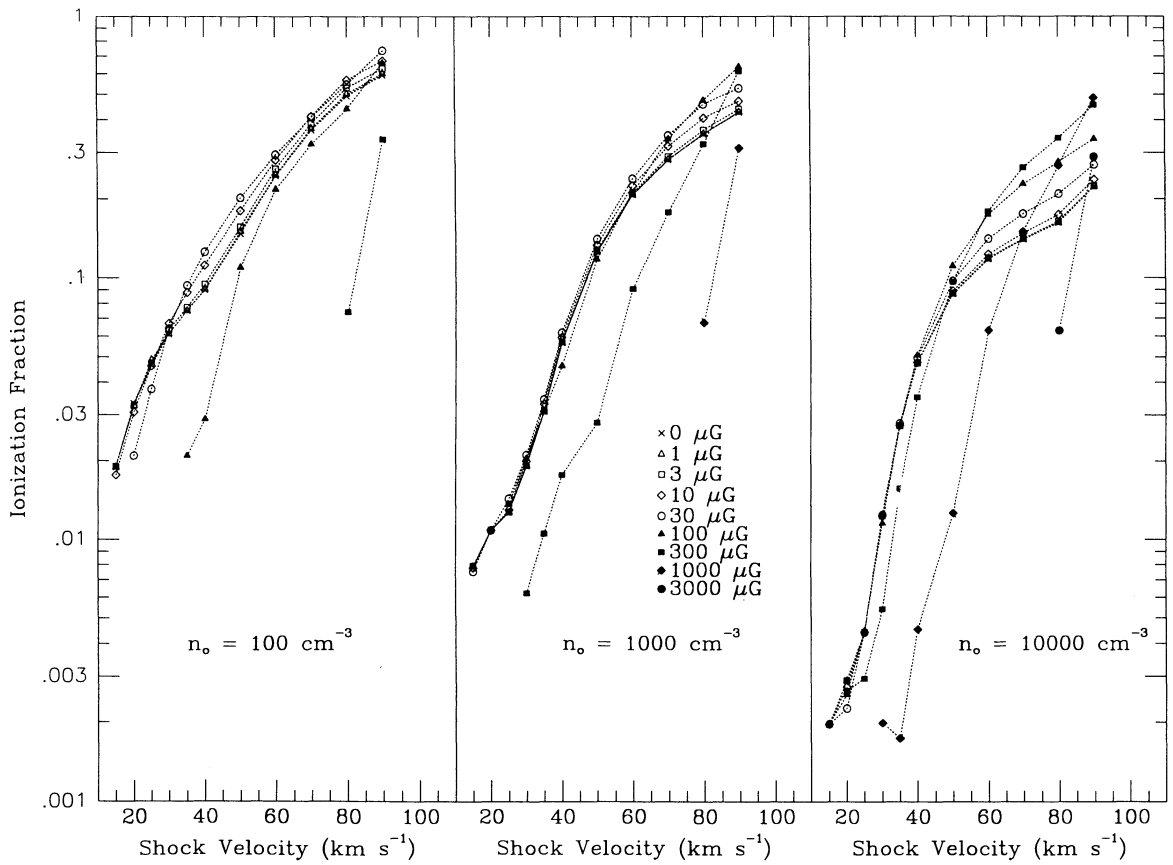

FIG. 16.—The [S II]–weighted ionization fraction is plotted against shock velocity for each of our models. Low shock velocities have low ionization fractions.

4.1. *HH 34*

The jet and bow shocks in HH 34 are a classic example of a collimated supersonic flow. HH 34 consists of a nearly linear jet that lies within $\sim 30''$ from the exciting source, and a series of bow shocks located at greater distances from the source (Reipurth et al. 1986; Mundt et al. 1987; Heathcote & Reipurth 1992). Line emission from the bow-shaped object HH 34S has a component from the bow shock and another component from the Mach disk that decelerates the jet (Morse et al. 1992).

The relevant observational data needed to estimate the mass loss rate in HH 34 appear in Table 1 and Table 2. We have adopted the dereddened line ratios of Morse et al. (1993b) in Table 1 except for the [N II] line, which is less contaminated by Hα in the spectra of Reipurth et al. (1986). The electron density in Table 2 corresponds to the value derived from the diagnostic curves of Czyzak, Keyes, & Aller (1986) using the [S II] line ratio in Reipurth et al. (1986). The HH 34 jet has a component with low radial velocities and low electron densities, and a component with high radial velocities and high electron densities (Heathcote & Reipurth 1992); the value of 650 cm^{-3} in Table 2 represents an average for both components. Velocities in HH 34 are well known (Heathcote & Reipurth 1992), as is the size of the jet (Raga, Mundt, & Ray 1991). The luminosity of the [O I] λ6300 line in HH 34 was measured by Morse et al. (1993b) in an aperture of size $\sim 2''$.

Before we can convert each of the line ratios in Table 1 to a [S II]–weighted ionization fraction $\langle I \rangle$ and a shock velocity V_S we need to estimate an approximate preshock density so we know which of the three panels to use in Figures 3–12. A quick glance at the figures shows that "low-excitation" knots (Böhm et al. 1980) like those in HH 34 have $\langle I \rangle \sim 1\%$, and shock velocities $V_S \sim 30$ km s^{-1}. Hence, the total density in the emitting region is $\sim 6.5 \times 10^4$ cm^{-3}; taking into account the compression of ~ 15 for a 30 km s^{-1} shock (Fig. 17) we obtain a preshock density of ~ 4300 cm^{-3}. This approximate calculation shows that we should use the panels labeled $n_0 = 1000$ and $n_0 = 10{,}000$ in Figures 3–12.

Ionization fractions derived from each of the observed line ratios appear in Table 3. Values for $\langle I \rangle$ range between 0.9% and 2.6% and are *almost an order of magnitude lower* than previous estimates (e.g., Raga 1991). Shock velocities for HH 34 calculated from four different line ratios (Table 4) lie in a narrow range between 25 km s^{-1} and 33 km s^{-1}. The compression derived from the average shock velocity and the curves in Figure 17 is 15.7. Correcting the observed electron density for the ionization and the compression (eq. [2]), we find that the average density in the jet is 1.0×10^4 cm^{-3} (Table 5).

Using equation (4) for the HH 34 jet we obtain a mass-loss rate of $1.7 \times 10^{-7}\ M_\odot$ yr^{-1}. The mass-loss rate found from equation (12) using the [O I] λ6300 luminosity estimate of Morse et al. (1993b) is $1.5 \times 10^{-7}\ M_\odot$ yr^{-1}. The nearly exact

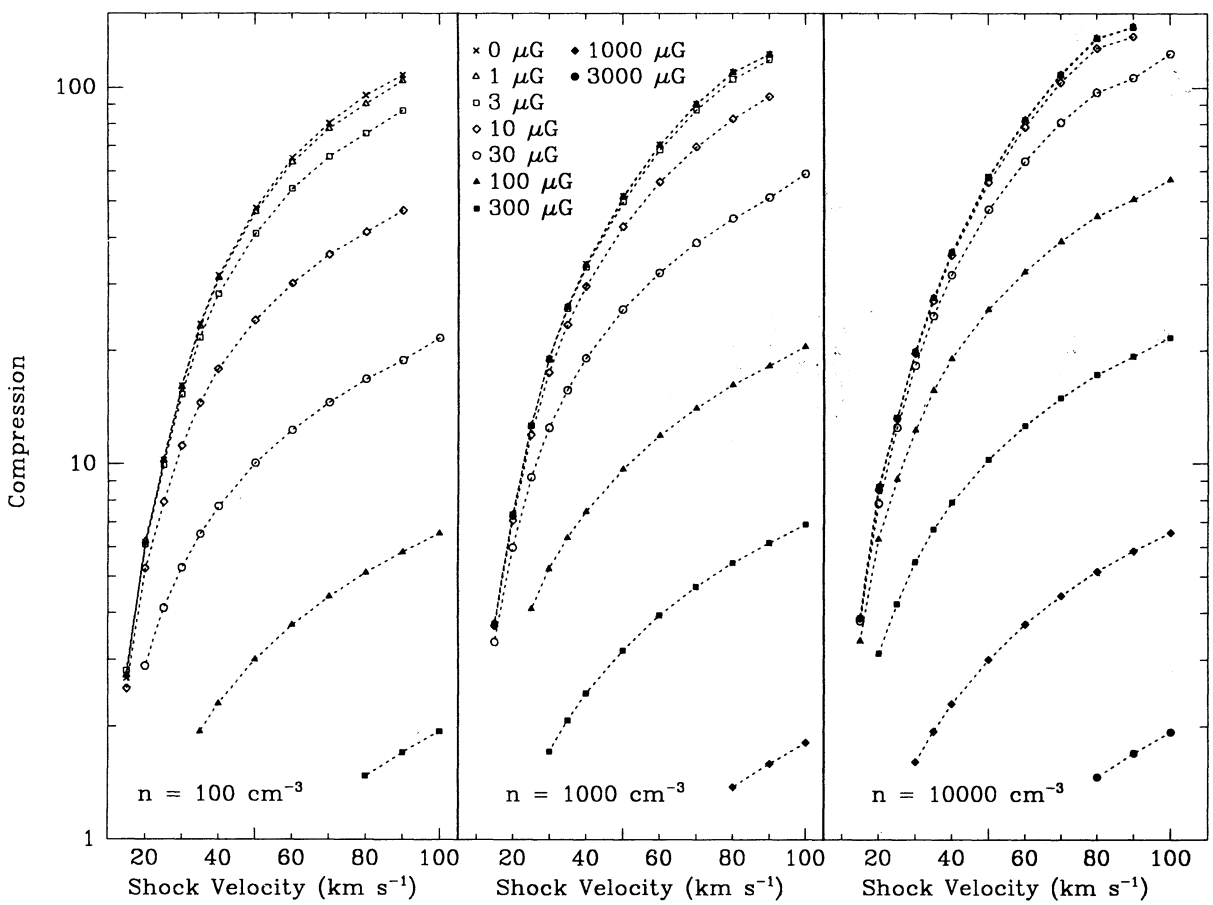

FIG. 17.—The [S II]–weighted compression (see eq. [3]) is plotted against shock velocity for each of our models. The compression increases with shock velocity and decreases when a magnetic field is present.

TABLE 1

OBSERVED LINE RATIOS (DEREDDENED)

Object	[O I] λ6300 / Hα	[S II] λλ6723 / Hα	[N I] λλ5200 / Hβ	[N II] λ6583 / [O I] λ6300	[N I] λλ5200 / [N II] λ6583	References
HH 34 (C–K)	2.3	6.1	3.4	0.08	4.4	1, 2
HH 47 (B_3–B_{11})	0.92	1.8	1.9	0.20	1.8	3
HH 111 (D–J)	1.3	2.9	2.1	0.19	2.5	1, 4

REFERENCES.—(1) Morse et al. 1993b; (2) Reipurth et al. 1986; (3) Morse et al. 1994; (4) Reipurth 1989b.

TABLE 2

OBSERVED VELOCITIES, DENSITIES, AND LUMINOSITIES

Object	N_e (cm^{-3})	V_J (km s^{-1})	$V_\perp$ (km s^{-1})[a]	Jet Area (cm^2)	$L_{[O\ I]\lambda 6300}$ ($L_\odot$)	$l_\perp$ (cm)[b]	References
HH 34 (C–K)	650	220	195	2.4×10^{31}	1.15×10^{-4}	1.4×10^{16}	1, 2, 3, 4, 5
HH 47 (B_3–B_{11})	250	350	320	2.4×10^{32}	9.3×10^{-4}	1.4×10^{17}	1, 6, 7
HH 111 (D–J)	900	320	315	2.4×10^{31}	5.8×10^{-4}	2.1×10^{16}	1, 5, 8, 9

[a] Tangential component of the jet velocity.

[b] Size of aperture used to measure the [O I] λ6300 luminosity.

REFERENCES.—(1) Czyzak, Keyes, & Aller 1986; (2) Reipurth et al. 1986; (3) Heathcote & Reipurth 1992; (4) Raga, Mundt, & Ray 1991; (5) Morse et al. 1993b; (6) Morse et al. 1994; (7) Reipurth & Heathcote 1991; (8) Reipurth, Raga, & Heathcote 1992; and (9) Osterbrock 1989.

TABLE 3

IONIZATION FRACTION $\langle I \rangle$[a]

Object	[O II] λ6300 / Hα	[S II] λλ6723 / Hα	[N I] λλ5200 / Hβ	[N II] λ6583 / [O I] λ6300	[N I] λ5200 / [N II] λ6583	Average $\langle I \rangle$
HH 34	0.009	0.009	0.013	0.026	0.023	0.016
HH 47	0.023	0.030	0.025	0.055	0.050	0.036
HH 111	0.014	0.016	0.017	0.052	0.034	0.027

[a] Ionization fraction computed from the observed line ratios in Table 1 and the curves in Figs 3–7. The observed electron densities N_e must be divided by the ionization fraction $\langle I \rangle$ and then corrected for the compression $\langle C \rangle$ to give the average density $\langle N \rangle$ in the jet (see Table 5).

TABLE 4

SHOCK VELOCITIES

Object	[O I] λ6300 / Hα	[S I] λλ6723 / Hα	[N I] λλ5200 / Hβ	[N II] λ6583 / [O I] λ6300	Average V_S
HH 34	25	25	29	33	28
HH 47	31	34	32	39	34
HH 111	29	30	30	39	32

[a] The shock velocities found from the observed line ratios and the curves in Figs. 8–12.

TABLE 5

COMPRESSION, AVERAGE DENSITIES

Object	$\langle C \rangle$[a]	$\langle N \rangle$ (cm^{-3})[b]
HH 34	16	1.2×10^4
HH 47	24	1.4×10^3
HH 111	22	7.1×10^3

[a] The compression produced by a shock velocity V_S given in Table 4 according to the curves in Fig. 17. Large magnetic fields reduce the compression (see § 4.4).

[b] $\langle N \rangle = N_e \langle C \rangle^{-1/2} \langle I \rangle^{-1}$ is the average density in the flow. The $\langle I \rangle$ term converts the observed electron density to the total density, and the $\langle C \rangle$ term corrects the total density for compression.

agreement is fortuitous, but it is encouraging that these two independent methods give similar answers.

Our value for the mass-loss rate in HH 34 is *a factor of 200 higher* than the rate estimated by Mundt et al. (1987). The low ionization fraction accounts for a factor of ~60, and by using $\langle C \rangle^{1/2}$ instead of $\langle C \rangle$ to correct for compression we obtain an additional factor of 4 increase in $\dot{M}_{out}$. Our mass-loss rate for HH 34 is ~50% higher than the estimate of Raga (1991), who used an ionization fraction of 10% (a factor of 6 too large, according to Table 3). Overestimating the ionization fraction leads to a mass-loss rate that is too small, but Raga did not correct for compression in his estimate, which overestimates the mass-loss rate by a factor $\sim \langle C \rangle^{1/2} = 4$. As we noted in § 2.1, one must correct for compression because the mass flux

in the postshock gas does not represent a good average for the flow (see Fig. 2).

It is possible to estimate the rate of disk accretion onto young stars within a factor of ~ 2 by measuring the ratio of the excess continuum caused by accretion to the photospheric flux (Basri & Batalha 1990; Hartigan et al. 1991). This method works only if photospheric absorption is present in the object, which is not the case for HH 34 IRS. Hence, we estimate the mass accretion rate in HH 34 IRS by assuming that all of the observed luminosity in the infrared comes from accretion:

$$L_{\rm IR} = \frac{GM_* \dot{M}_{\rm acc}}{2R_*} \tag{11}$$

or

$$\dot{M}_{\rm acc} = 2.4 \times 10^{-7} \left(\frac{R_*}{2.1 \times 10^{11}\ {\rm cm}}\right)\left(\frac{L_{\rm IR}}{L_\odot}\right) \times \left(\frac{M_*}{0.8\ M_\odot}\right)^{-1} M_\odot\ {\rm yr}^{-1}\ . \tag{12}$$

Unfortunately, we cannot estimate M_* or R_* accurately for HH 34 IRS owing to the lack of photospheric lines. Adopting $M_* = 0.8\ M_\odot$ and $R_* = 2.1 \times 10^{11}$ cm, and using $L_* = 45\ L_\odot$ (Cohen & Schwartz 1987), the mass accretion rate from equation 12 is $1.1 \times 10^{-5}\ M_\odot\ {\rm yr}^{-1}$. Note that the mass in the jet was ejected from the star ~ 200 yr ago; it is quite possible that the mass accretion rate 200 yr ago was much higher than it is now.

The ratio of mass outflow to mass accretion in HH 34 IRS is $\sim 2\%$. The mechanical luminosity ($0.5\dot{M}V_J^2$) and momentum rate in the jet are listed in Table 6. The mechanical luminosity is about 2% of the luminosity of the source; the momentum supplied by the jet is $3.7 \times 10^{-5}\ M_\odot\ {\rm yr}^{-1}\ {\rm km\ s}^{-1}$, enough to power a weak molecular flow (Lada 1985). However, to date no molecular flows have been found around HH 34.

4.2. *HH 47*

The HH 47 jet emanates from a newly formed star at the center of a dark globule near the edge of the Gum nebula. Several bow shocks present in the flow are probably caused by time variability (Reipurth 1989a; Hartigan et al. 1990). Effects of entrainment are clear in the velocity structure and excitation of the jet (Hartigan et al. 1993).

The line ratios for HH 47 listed in Table 1 are taken for the bright section of the jet labeled B3–B11 by Reipurth & Heathcote (1991). The observed electron density of HH 47B3–B11 from Fabry-Perot observations is $\sim 250\ {\rm cm}^{-3}$ (Morse et al. 1994). The radial velocity of the jet with respect to the source is $\sim 150\ {\rm km\ s}^{-1}$ (Reipurth 1989a), which implies a true space velocity of $350\ {\rm km\ s}^{-1}$ and a tangential velocity of $\sim 320\ {\rm km\ s}^{-1}$ for an orientation angle of 65° (Morse et al. 1994). The jet is resolved spatially and has a diameter of 2.″6.

To estimate the ionization fraction and shock velocity we must first obtain a rough estimate of the density so we know which panels to use in Figures 3–12. The HH 47 jet has a somewhat higher excitation spectrum on average than the HH 34 jet, but the ionization fraction is still $\sim 2\%$, with a shock velocity of $\sim 30\ {\rm km\ s}^{-1}$. The compression is roughly a factor of 20, so the preshock density is ~ 2.5 times greater than the observed value of N_e ($250\ {\rm cm}^{-3}$) in the postshock region. Hence, we use the middle panel ($n_0 = 1000\ {\rm cm}^{-3}$) to estimate shock velocities and densities in Figures 3–12.

The ionization fraction in the HH 47 jet ranges between 0.023 and 0.055 for the five line ratios in Table 3. The shock velocities found from the line ratios lie between 31 km s^{-1} and 39 km s^{-1}. The ionization fractions and shock velocities we derive from ratios involving the [N II] λ6583 line are higher than those found from other line ratios, perhaps because the shocks in the jet are not exactly planar. The average ionization fraction in the HH 47 jet is 3.6% and the average shock velocity is 34 km s^{-1}. Using this shock velocity in Figure 17 we find a compression of 24. The average density $\langle N \rangle$ in the jet is then $1400\ {\rm cm}^{-3}$, and the mass loss rate is $3.9 \times 10^{-7}\ M_\odot\ {\rm yr}^{-1}$.

The [O I] luminosity over the 20″ section B3–B11 of the HH 47 jet is $9.3 \times 10^{-4}\ L_\odot$ from our Fabry-Perot observations (Hartigan et al. 1993). Using equation (10) we obtain a mass-loss rate of $4.2 \times 10^{-7}\ M_\odot\ {\rm yr}^{-1}$, which agrees extremely well with the estimate found using the average jet density.

The luminosity of the central source is dominated by accretion—a spectrum of the reflected light from HH 46 at the base of the jet shows only continuum (Graham & Heyer 1989). Cohen & Schwartz (1987) give the luminosity of the exciting star as $24\ L_\odot$, and using this value in equation (12) we find a mass accretion rate of $5.8 \times 10^{-6}\ M_\odot\ {\rm yr}^{-1}$ for HH 47 IRS. The mass outflow rate in the HH 47 jet is about 7% of the mass accretion rate. The mechanical luminosity in the jet is about one-sixth of the accretion luminosity of the source (Table 6).

The momentum rate in the jet is $1.4 \times 10^{-4}\ M_\odot\ {\rm yr}^{-1}\ {\rm km\ s}^{-1}$. The total momentum in the blueshifted lobe of the molecular flow is $0.5\ M_\odot\ {\rm km\ s}^{-1}$ (Chernin & Masson 1991); the jet supplies enough momentum to drive the molecular outflow if the outflow lasts $\gtrsim 3600$ yr. Adopting a tangential velocity of $\sim 230\ {\rm km\ s}^{-1}$ for the outer bow shock HH 47D, we find that the jet is at least 1000 yr old. The medium exterior to the outer bow shock also appears to move away from the source at several hundred km s^{-1} (Morse et al. 1994), so the lifetime of the jet probably exceeds 1000 yr. In 1000 yr the jet carries a total of 5.9×10^{44} ergs, more than an order of magnitude

TABLE 6

MASS LOSS, MASS ACCRETION, MOMENTUM LOSS, AND LUMINOSITIES

Object	$\dot{M}_{\rm out}$ [a]	$\dot{M}_{L([{\rm O\ I}])}$ [b]	$\dot{M}_{\rm acc}$ [c]	$\dot{M}_{\rm out}/\dot{M}_{\rm acc}$	$\dot{P}_{\rm jet}$ [d]	$L_{\rm jet}$ [e]	$L_{\rm BOL}$ [f]
HH 34	1.7×10^{-7}	1.5×10^{-7}	1.1×10^{-5}	0.015	3.7×10^{-5}	0.7	45
HH 47	3.9×10^{-7}	4.2×10^{-7}	5.8×10^{-6}	0.07	1.4×10^{-4}	4.1	24
HH 111	1.8×10^{-7}	5.8×10^{-7}	6.0×10^{-6}	0.03	5.8×10^{-5}	1.5	25

[a] $\dot{M}_{\rm out} = \mu m_{\rm H} \langle N \rangle V_J A$ is given in $M_\odot\ {\rm yr}^{-1}$.
[b] $\dot{M}_{L([{\rm O\ I}])}$ is the mass-loss rate found from the luminosity of [O I] λ6300 (eq. [1]), in $M_\odot\ {\rm yr}^{-1}$.
[c] Mass accretion rate (see text) in $M_\odot\ {\rm yr}^{-1}$.
[d] $\dot{P}_{\rm jet} = \dot{M}V_J$, measured in $M_\odot\ {\rm yr}^{-1}\ {\rm km\ s}^{-1}$.
[e] $L_{\rm jet} = \frac{1}{2}\dot{M}V_J^2$, measured in $L_\odot$.
[f] Total luminosity of the exciting source in $L_\odot$, including both accretion and photospheric components.

greater than the energy in the molecular flow (Chernin & Masson 1991). *We conclude that the jet in HH 47 carries sufficient momentum and energy to produce the observed molecular outflow.*

4.3. *HH 111*

The HH 111 jet was discovered by Reipurth (1989b), and is another example of a highly collimated jet with several bow shocks located in the flow. A section of the jet close to the star has a low-excitation spectrum and is suitable for the present analysis (Noriega-Crespo et al. 1993; Morse et al. 1993b). Proper motions and radial velocities for HH 111 have been discussed by Reipurth et al. (1992), who also measured the width of the jet. We use the line ratios in Reipurth (1989b) and Morse et al. (1993b) to derive the ionization fraction and shock velocity of the HH 111 jet. The electron densities quoted by Reipurth (1989b) are consistently higher than those found from the diagnostic curves of Czyzak et al. (1986) or Osterbrock (1989). Using the observed line ratio of [S II] λ6716/[S II] λ6731 = 0.83 for $T = 8200$ K we find $N_e \sim 900$ cm^{-3}. Hence, we use the panels labeled $n_0 = 1000$ and $n_0 = 10{,}000$ in Figures 3–12 to estimate ionization fractions and shock velocities.

The ionization fraction is about a factor of 2 higher for HH 111 than it is in HH 47 or HH 34, primarily because [N II] λ6583 is more prominent in HH 111. The larger [N II] flux in HH 111 introduces some scatter in the ionization fractions (Table 3), but each estimate lies within a factor of 2 of the average of 2.7%. Likewise the line ratio involving [N II] λ6583 in Table 4 gives a shock velocity that is somewhat higher than those inferred from other line ratios. Nevertheless, the uncertainty in the average shock velocity of 32 km s^{-1} is still only $\pm$4 km s^{-1}. The compression in the HH 111 jet (Fig 17) is 22, and the average density in the jet is $\langle N \rangle = 7100$ cm^{-3}. From these numbers we derive a mass loss rate of $1.8 \times 10^{-7}\ M_\odot$ yr^{-1} for HH 111.

The total Hα luminosity in a 3″ aperture centered on knot L is $\sim 9 \times 10^{-4}\ L_\odot$ (Morse et al. 1993b). The flux of Hα is about a factor of two lower in the main part of the jet (knots D–J), and using the observed line ratios (Table 1) we obtain $L_{[O\ II]} = 5.8 \times 10^{-4}\ L_\odot$. Equation (10) gives a mass-loss rate of $5.8 \times 10^{-7}\ M_\odot$ yr^{-1}, about a factor of 3 higher than that found from analysis of the densities in the jet.

The exciting source of HH 111 is not visible at optical wavelengths, so we must again use equation (12) to estimate a mass accretion rate. The luminosity of HH 111 IRS is 25 $L_\odot$ (Reipurth & Olberg 1991), corresponding to a mass accretion rate of $\dot{M}_{acc} = 6.0 \times 10^{-6}\ M_\odot$ yr^{-1}. The mass outflow rate is 3% of the mass accretion rate in HH 111. The mechanical luminosity in the jet is 1.5 $L_\odot$, or 6% of the luminosity of the source.

A bipolar molecular outflow in HH 111 has recently been discovered by Reipurth & Olberg (1991) to lie along the direction of the optical jet. The mass in the blueshifted portion of the molecular flow is about 0.1 $M_\odot$. The momentum in the molecular flow equals the mass times a characteristic velocity. The observed average radial velocity of the blueshifted gas is about 2.5 km s^{-1} with respect to the ambient cloud. However, this radial velocity is probably lower than the average space velocity of the gas because the HH 111 flow lies nearly in the plane of the sky. If we correct for the inclination of the HH 111 flow we obtain a velocity of $\sim$10 km s^{-1} for the molecular flow, which implies that the momentum in the blueshifted molecular flow is 1.0 $M_\odot$ km s^{-1}.

The jet carries enough momentum to derive the molecular flow in about 1.7×10^4 yr. The outer bow shock HH 111V is only about 800 yr old (Reipurth et al 1992), but this bow shock is not the first ejection in the jet; the gas exterior to HH 111V also moves at a high velocity with respect to the exciting source (Morse et al. 1993a). We cannot estimate the age of the jet reliably from existing optical data because we cannot identify the first ejection in the jet. The dynamical timescale for the outflow is 5.4×10^4 yr (Reipurth & Olberg 1991), so the jet can drive the molecular flow if the jet is nearly as old as the molecular flow. The kinetic energy of the jet (1.5 $L_\odot$) can easily account for the energy carried by the molecular flow (0.055 $L_\odot$).

4.4. *Estimating the Magnetic Field in Jets from Line Ratios*

The [S II]–weighted compression $\langle C \rangle$ (Fig. 17) decreases markedly if the component of the magnetic field $B_\parallel$ that lies parallel to the surface of the shock becomes large. Even shocks with moderate fields have enough magnetic pressure in the postshock regions to inhibit the compression of the gas as it cools. Likewise, the total flux of Hβ produced behind the shock depends on $B_\parallel$ (Fig. 15). Figures 15, 17, and 18 suggest that it might be possible to estimate $B_\parallel$ from observations of the electron density, the shock velocity, and the line fluxes in jets.

Unfortunately, the emission line ratios obtained from shocks with large values of $B_\parallel$ closely resemble the ratios found from lower velocity shocks without fields. For example, Table 7 shows the line ratios and fluxes for a 30 km s^{-1} shock model with a small field, and a 50 km s^{-1} model with $B_\parallel = 1$ mG. The line ratios are essentially identical for the two models. The compression is a factor of 6 lower in the model with the large field, and so this model must have a higher preshock density to produce the same electron density as the lower velocity shock with a small field. The ionization fraction is nearly the same in both cases (the ionization fraction found from the ratio [N II] λ6583/[O I] λ6300 in Fig. 6 is essentially independent of the preshock density and the preshock magnetic field).

One major difference between the two models in Table 7 is that the high field model has a larger Hβ flux than the low field model. This difference is caused by the higher preshock density in the 50 km s^{-1} model—more atoms pass through this shock and so the total amount of radiated energy is higher for this case. However, we cannot use the Hβ fluxes to estimate $B_\parallel$

TABLE 7

EFFECT OF MAGNETIC FIELDS ON LINE RATIOS

Parameter	Large Field Model	Small Field Model
$B_\parallel$ (μG)[a]	1000	1
n_0 (cm^{-3})	1.0×10^5	1.08×10^4
V_S (km s^{-1})	50	30
[S II] λ6716/[S II] λ6731	1.11	1.11
[O I] λ6300/Hα	0.97	1.1
[S II] $\lambda\lambda$6723/Hα	2.4	2.7
[N I] $\lambda\lambda$5200/Hβ	2.2	2.5
[N II] λ6583/[O I] λ6300	0.036	0.053
N_e (cm^{-3})	390	390
$F_{(H\beta)}$ (ergs cm^{-2} s^{-1})	4.4×10^{-4}	4.2×10^{-5}
$\langle C \rangle$[b]	3.0	19
$\langle I \rangle$[b]	0.013	0.019
$\langle N \rangle$ (cm^{-3})[b]	1.7×10^4	4.4×10^3

[a] Component of the preshock magnetic field that lies parallel to the surface of the shock.

[b] As defined in Tables 1–6.

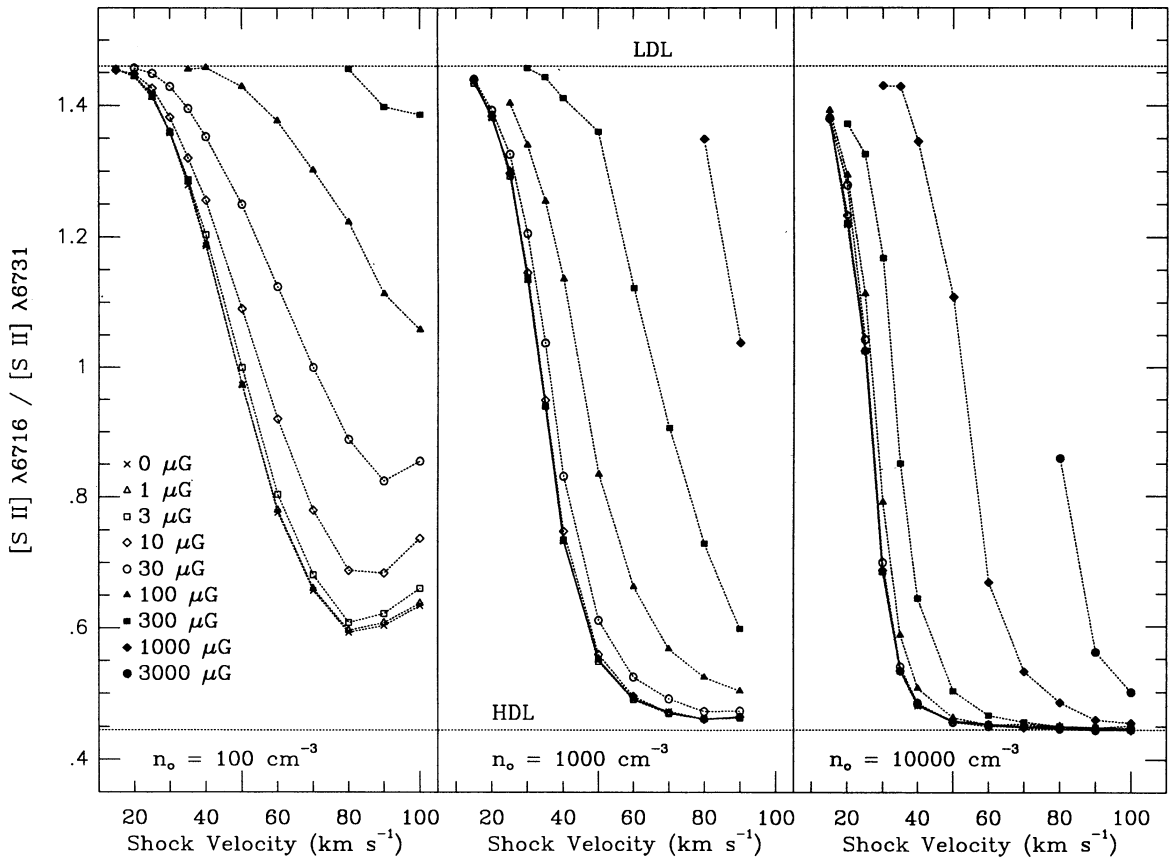

FIG. 18.—The ratio of [S II] λ6716/[S II] λ6731 is shown as a function of shock velocity for each of our models. The labels "LDL" and "HDL" denote the low-density limit and the high-density limit, respectively. Like the compression in Fig. 17, the [S II] line ratio depends upon the magnetic field. If the shock velocity can be estimated accurately from observations of other line ratios, this figure provides a means to convert an observed [S II] line ratio to an estimate of the preshock magnetic field.

unless we know the total area of the shocks in the jet. For example, a stationary oblique shock covers much more surface area than a nonstationary normal shock, though the effective shock velocity can be the same in both cases. Without very high spatial resolution images, we cannot know if the emission contained in a 2″ aperture arises from one dense magnetic shock or several less dense nonmagnetic shocks.

4.5. *Discussion*

An extended, low-velocity component often surrounds the high-velocity gas located along the axis of stellar jets (e.g., Solf 1987; Hartigan et al. 1993), and the electron densities and line ratios in this low-velocity gas often differ from those of the high-velocity gas (Heathcote & Reipurth 1992; Morse et al. 1993b). The most likely origin of the two velocity components is that the high-velocity gas entrains slower material from the edges of the jet. In this paper we have ignored entrainment and have taken averages of the total emission to compute mass-loss rates. Emission lines from any planar shock, regardless of the physical origin of the shock, provide a measure of the ionization fraction and shock velocity in the jet. Our models can be used to descibe those portions of the jet characterized by a single effective shock velocity even if the geometry of the shocks is complicated. The geometry of the shocks in the jet, particularly where entrainment occurs, could be quite complex.

Mass-loss rates found from the luminosity of the [O I] λ6300 line and those calculated from the densities and ionization fractions in jets agree remarkably well (Table 6). All three of the jets discussed above have enough momentum and energy to power a weak molecular flow. In fact, if we plot the momentum rate in the jet against the luminosity of the central source (e.g., Lada 1985) we find that the HH 34, HH 47, and HH 111 jets occupy the same region of the diagram as the less energetic molecular flows. Whether or not jets power the most energetic molecular outflows is uncertain, though jets have been observed around massive stars (e.g., Ray et al. 1990).

Although the rotational velocities of the exciting stars of HH 34, HH 47, and HH 111 are unknown, other young stars rotate at only a small fraction of the breakup speed (Hartmann et al. 1986; Bouvier et al. 1986). Recent models show that magnetized flows from young stars where $\dot{M}_{\rm out} \gtrsim 0.1\dot{M}_{\rm acc}$ remove the angular momentum accreted through the disk provided that the Alfvén radius of the flow is large enough to provide enough torque to keep the star spinning slowly (Shu et al. 1993; Pelletier & Pudritz 1992). Table 6 shows that the jets of HH 34, HH 47, and HH 111 remove 1%–10% of the mass accreted onto the central object. Hence, jets may remove large amounts of angular momentum from the central object if they originate with a substantial nonradial velocity component.

5. CONCLUSIONS

We have calculated an extensive grid of radiative shock models that cover the range of magnetic fields, shock velocities, and densities relevant to emission lines in stellar jets. Our

primary goal for these calculations was to estimate the ionization fraction and shock velocity of the knots in the jet from the observed line ratios. The ionization fraction allows us to convert the observed electron density to a total density, and thereby estimate the mass and momentum carried in the flow. Our principal results are as follows:

1. Mass fluxes in stellar jets are not constant; even if the flow originates with a constant mass flux, it will evolve into a clumpy flow if the velocity varies along the jet. The mass fluxes are highest in the postshock regions of the flow and lowest in the preshock regions. Hence, mass-loss rates found from densities in the postshock regions of the flow must be corrected for compression. We compute the mass-loss rate from a geometric mean of the preshock and postshock densities.

2. The ionization fractions in the forbidden line–emitting regions of stellar jets are only about 2%, much smaller than estimated previously.

3. Shock velocities in the jets are typically 30 km s^{-1}. Shock models can reproduce the low excitation spectra observed in stellar jets.

4. The average mass-loss rate found from the luminosity of the [O I] λ6300 line agrees remarkably well with those from the densities in jets. Mass-loss rates from the optically visible portions of jets are $\gtrsim 2 \times 10^{-7}\ M_\odot\ \mathrm{yr}^{-1}$, *roughly two orders of magnitude higher than those found by* Mundt et al. (1987). These mass loss rates are typically 1%–10% of the mass accretion rate.

5. Jets carry enough energy and momentum to power small molecular ouflows. In particular, the HH 47 jet can supply the momentum and energy of the observed molecular outflow in about 3600 yr. The HH 111 jet may also power the molecular outflow in this region if the age of the jet is comparable to the dynamical age of the molecular flow.

6. We were unable to determine the magnetic field in stellar jets because the line ratios from a shock with a large magnetic field resemble those from a lower velocity, lower density shock without a field. It may be possible to estimate a field strength from the total flux of the emitting gas, provided enough is known about the geometry of the shocks in the flow.

We are grateful to John Kwan for emphasizing the importance of [O I] luminosities to determine mass-loss rates. We also thank Steve Strom and Suzan Edwards for helpful comments during the course of this work. P. H. was supported by grants NSF AST 91-14863, NASA NAGW-1417, and NASA NAG 2-462 to S. Strom during the course of this work, and J. M. was funded by NASA grants NAGW-2689 and NAGW-3268 to A. Wilson at STScI. We are grateful to John Slavin for pointing out the error in the [S II] excitation rate.

REFERENCES

Basri, G., & Batalha, C. 1990, ApJ, 363, 654
Basri, G., & Bertout, C. 1993, in Protostars and Planets III, ed. G. Levy & J. Lunine (Tucson: Univ. Arizona Press), 543
Böhm, K.-H., Brugel, E., & Mannery, E. 1980, ApJ, 235, L137
Bouvier, J., Bertout, C., Benz, W., & Mayor, M. 1986, A&A, 165, 110
Cabrit, S., Edwards, S., Strom, S., & Strom, K. 1990, ApJ, 354, 687
Carr, J. 1993, ApJ, 406, 553
Chernin, L., & Masson, C. 1991, ApJ, 382, L93
Cohen, M., & Schwartz, R. 1987, ApJ, 316, 311
Cox, D., & Raymond, J. 1985, ApJ, 298, 651
Croswell, K., Hartmann, L., & Avrett, E. 1987, ApJ, 312, 227
Czyzak, S., Keyes, C., & Aller, L. 1986, ApJS, 61, 159
Davis, C., Dent, W., Matthews, H., Aspin, C., & Lightfoot, J. 1993, MNRAS, in press
Edwards, S., Cabrit, S., Strom, S., Heyer, I., Strom, K., & Anderson, E. 1987, ApJ, 321, 473
Edwards, S., et al. 1993, AJ, 106, 372
Edwards, S., Ray, T., & Mundt, R. 1993, in Protostars and Planets III, ed. G. Levy & J. Lunine (Tucson: Univ. of Arizona Press), 567
Eislöffel, J., & Mundt, R. 1992, A&A, 263, 292
Gouveia Dal Pino, E., & Benz, W. 1994, ApJ, submitted
Graham, J., & Heyer, M. 1989, PASP, 101, 573
Hartigan, P., Kenyon, S., Hartmann, L., Strom, S., Edwards, S., Welty, A., & Stauffer, J. 1991, ApJ, 382, 617
Hartigan, P., Morse, J., Heathcote, S., & Cecil, G. 1993, ApJ, 414, L121
Hartigan, P., & Raymond, J. 1993, ApJ, 409, 705
Hartigan, P., Raymond, J., & Curiel, S. 1989, ApJ, 347, L31
Hartigan, P., Raymond, J., & Hartmann, L. 1987, ApJ, 316, 323
Hartigan, P., Raymond, J., & Meaburn, J. 1990, ApJ, 362, 624
Hartmann, L., Hewett, R., Stahlar, S., & Mathieu, R. D. 1986, ApJ, 309, 275
Heathcote, S., & Reipurth, B. 1992, AJ, 104, 2193
Kepner, J., Hartigan, P., Yang, C., & Strom, S. 1993, ApJ, 415, L119
Kwan, J., & Tademaru, E. 1988, ApJ, 337, 903
Lada, C. 1985, ARA&A, 23, 267
Lind, K., Payne, D., Meier, D., & Blandford, R. 1989, ApJ, 344, 89
Lovelace, R., Romanova, M., & Contopoulous, J. 1993, ApJ, 403, 158
Masson, C. R., & Chernin, L. M. 1993, ApJ, 414, 230
Mendoza, C. 1983, in IAU Symp. 103, Planetary Nebulae, ed. D. R. Flower (Dordrecht: Reidel), 143
Morse, J., Hartigan, P., Cecil, G., Raymond, J., & Heathcote, S. 1992, ApJ, 399, 231
Morse, J., Hartigan, P., Heathcote, S., Raymond, J. C., & Cecil, G. 1994, ApJ, 425, 738
Morse, J., Heathcote, S., Cecil, G., Hartigan, P., & Raymond, J. 1993a, ApJ, 410, 764
Morse, J., Heathcote, S., Hartigan, P., & Cecil, G. 1993b, AJ, 106, 1139
Mundt, R., Brugel, E., & Bührke, T. 1987, ApJ, 319, 275
Noriega-Crespo, A., Garnavich, P., & Raga, A. 1993, AJ, 106, 1133
Osterbrock, D. 1989, Astrophysics of Gaseous Nebulae and Active Galactic Nuclei (Mill Valley: University Science Books)
Pelletier, G., & Pudritz, R. 1992, ApJ, 394, 117
Raga, A. C. 1991, AJ, 101, 1472
Raga, A., Binette, L., & Cantó, J. 1990, ApJ, 360, 612
Raga, A., & Cabrit, S. 1993, A&A, 278, 627
Raga, A., Cantó, J., Calvet, N., Rodríguez, L., & Torrelles, J. 1993, A&A, 276, 539
Raga, A., Mundt, R., & Ray, T. 1991, A&A, 252, 733
Ray, T., Pötzel, R., Solf, J., & Mundt, R. 1990, ApJ, 357, L45
Raymond, J. 1979, ApJS, 39, 1
Reipurth, B. 1989a, in Low Mass Star Formation and Pre–Main-Sequence Objects, ed. B. Reipurth (Garching: ESO), 247
———. 1989b, Nature, 340, 42
Reipurth, B., Bally, J., Graham, J., Lane, A., & Zealey, W. 1986, A&A, 164, 51
Reipurth, B., & Heathcote, S. 1991, A&A, 246, 511
Reipurth, B., & Olberg, M. 1991, A&A, 246, 535
Reipurth, B., Raga, A., & Heathcote, S. 1992, ApJ, 392, 145
Shu, F., Lizano, S., Ruden, S. P., & Najita, J. 1988, ApJ, 328, L19
Shu, F., Najita, J., Galli, D., Ostriker, E., & Lizano, S. 1993, in Protostars and Planets III, ed. G. Levy & J. Lunine (Tucson: Univ. of Arizona Press), 3
Solf, J. 1987, A&A, 184, 322
Solf, J., & Böhm, K.-H. 1987, AJ, 93, 1172
Stahler, S. 1994, ApJ, 422, 616
Stocke, J., et al. 1988, ApJS, 68, 229
Zealey, W., Suters, M., & Randall, P. 1993, Proc. Astron. Soc. Australia, in press